IEEE Access
Multidisciplinary ⋮ Rapid Review ⋮ Open Access Journal

Received 13 February 2023, accepted 27 March 2023, date of publication 11 April 2023, date of current version 14 April 2023.

Digital Object Identifier 10.1109/ACCESS.2023.3266272

RESEARCH ARTICLE

Multi-Objective Finite-Frequency H_∞/GH_2 Static Output-Feedback Control Synthesis for Full-Vehicle Active Suspension Systems: A Metaheuristic Optimization Approach

YEONGJAE KIM[1], TAEHEON KWAK[1], MASAAKI KANNO[2], AND TAE-HYOUNG KIM[1], (Member, IEEE)

[1]Department of Mechanical Engineering, Chung-Ang University, Dongjak-gu, Seoul 06974, Republic of Korea
[2]Institute of Science and Technology, Academic Assembly, Niigata University, Nishi-ku, Niigata-shi 950-2181, Japan

Corresponding author: Tae-Hyoung Kim (kimth@cau.ac.kr)

This work was supported in part by the National Research Foundation of Korea (NRF) funded by the Korean Government (MSIT; Ministry of Science and ICT) under Grant 2021R1A2C1008686; and in part by the Chung-Ang University Graduate Research Scholarship in 2021.

ABSTRACT In this paper, the problem of multi-objective control for active suspension systems with polytopic uncertainty is addressed via H_∞/GH_2 static output feedback with a limited-frequency characteristic. For the overall analysis of the performance demanding both the vehicle-ride comfort related to vertical- and transversal-directional dynamics and the time-domain constraints related to the driving maneuverability, a seven-degree-of-freedom full-vehicle model with an active suspension system is investigated. The robust static output-feedback control strategy is adopted because some state variables may not be directly measured in a realistic implementation. In designing this control, the finite-frequency H_∞ performance using the generalized Kalman–Yakubovich–Popov lemma is optimized to improve the passenger's ride comfort, while the GH_2 performance is optimized to guarantee the constraints concerning the suspension deflection limitation, road-holding ability, and actuator saturation problem. This control synthesis problem is formulated as non-convex bilinear matrix inequalities and requires simultaneous consideration of different finite-frequency domain ranges for vertical and transversal motions for evaluating the H_∞ performance. These design difficulties are overcome by the proposed multi-objective quantum-behaved particle swarm optimizer, which efficiently explores the relevant trade-offs between the considered multiple performance objectives and eventually provides the desired set of Pareto-optimal solutions. Further, the numerical simulation cases of a full-vehicle active suspension system are presented to illustrate the effectiveness of the proposed control synthesis methodology in both frequency and time domain.

INDEX TERMS Active suspension system, static output feedback, finite frequency, generalized Kalman–Yakubovich–Popov lemma, bilinear matrix inequalities, multi-objective metaheuristic algorithm.

I. INTRODUCTION

An active suspension system is implemented to isolate the vibration and shock transmitted from uneven-road-surface interference to the vehicle body in terms of the comport of the passengers and potentially to ensure time-domain constraints such as suspension dynamic travel and road-holding property related to driving maneuverability. In recent decades, several advanced active-control strategies have been developed by introducing various techniques such as adaptive control [1], [2], fuzzy control [3], [4], [5], linear-quadratic-regulator control [6], [7], and sliding mode control [8], [9]. In particular, the comfort-oriented H_∞ active suspension control is considered the most powerful design alternative; therefore,

The associate editor coordinating the review of this manuscript and approving it for publication was Haibin Sun.

it has been intensively examined in the context of the attenuation of road-roughness-related disturbance and the robustness against model uncertainties [10], [11], [12], [13], [14].

There are two main aspects of the design specifications for developing active suspension systems. One is vehicle-ride comfort, which refers to the ability of a vehicle to insulate its passengers from road-induced vibrations. The other is the time-domain constraints for the driving maneuverability, which includes limiting suspension stroke to keep suspension displacement within an permissible range, limiting wheel hop to ensure continuous contact of the wheels with the road and limiting the actuator power to maintain the safety of the active suspension system [15]. In the design procedure, the H_∞ norm of the transfer function from the uneven road disturbance to the vehicle body acceleration is usually adopted to specify the ride-comfort performance, whereas the generalized H_2 (GH_2) norm is introduced to handle suspension deflection, road-holding ability, actuator saturation, etc. However, the two aforementioned design aspects are usually conflicting, e.g., excessive suspension displacement may occur if enhanced ride comfort is strongly required. Therefore, there is extensive literature mentioning the importance of multi-objective optimal control strategies to manage the trade-off between the two conflicting performance requirements. Nevertheless, until recently, most of the existing active suspension problems were handled piecemeal by H_∞ control theory, which only employs the H_∞ norm index for appropriately measuring the vibration suppression performance (e.g., refer to [10], [11], [12], [13], [14], [16], and [17] and the references therein).

Although various control strategies for isolating the vibration transmitted to passengers have been proposed, most of those studies have been concentrated on the controller design over the entire frequency range [18]. However, according to ISO 2631 [19], the human body is considerably sensitive to vibrations between 4Hz and 8Hz in the vertical direction, and human organs resonate with the vibrations belonging to such a frequency domain [18], [20]. From this viewpoint, the major focus of this research is to design a controller for attenuating the body acceleration along the vertical direction and optimizing the vehicle-ride comfort, particularly in the frequency band of 4–8 Hz. In this line of recent research, the generalized Kalman–Yakubovich–Popov (KYP) lemma [21] is adopted to handle targeted disturbance rejection via the H_∞ norm over a specific frequency band (see [18] and [22] and references therein). However, for the ride comfort of a vehicle's passengers, another critical problem is that the human body is also sensitive to vibrations caused by the transversal motion (i.e., roll motion) of the vehicle in the frequency domain of 0.5-2 Hz. Thus, to handle the finite-frequency control objective of vertical- and transversal-directional motions of a vehicle simultaneously, a full-car active suspension system should be adopted. Nevertheless, most of the existing controller designs are based on quarter- or half-car active suspension models; therefore, in the designing procedure, they cannot rigorously consider the fact that a human body subjected to the vehicle's rolling motion is very sensitive to vibrations in a certain finite-frequency band that is different from that for vertical vehicle motion. Although Jing et al. [18] recently introduced a full-car active suspension model, the transversal motion of the vehicle was not directly manipulated by the finite-frequency control; instead, some transversal-motion-related normalization factors were just handled as constraints during the vertical-directional controller design.

In the case of an active suspension system, some of the state variables of a vehicle cannot be measured or are difficult to directly measure in a practical situation; e.g., tire deflection cannot be measured or is not simple to measure in realistic implementation. This fact implies that the realization of an active suspension system with the usual state-feedback control mechanism may be a considerably cumbersome task. From this viewpoint, to improve the usability of an active vehicle suspension, static output-feedback (SOF) control can be adopted as a remedy methodology, which takes advantage of the state-feedback's simplicity while using a small number of signal types that are realistically measurable online. Unfortunately, while the state-feedback control problem can be simply solved using linear matrix inequalities (LMIs), the synthesis conditions of the output-feedback case are intrinsically non-convex and result in bilinear matrix inequalities (BMIs), which make it difficult to find a feasible solution set. Furthermore, the simultaneous consideration of two different finite-frequency domain ranges—4–8 Hz for vertical motion and 0.5–2 Hz for transversal motion— makes the multi-objective optimal SOF control synthesis a more challenging task. There have been some efforts to develop multi-objective SOF control for vehicle suspension systems. For example, Du and Zhang [23] proposed the H_∞/GH_2 controller design technique, and Han and Zhao [24] proposed the H_2/GH_2 controller design technique. However, their control techniques that enhance vehicle-ride comfort over the entire frequency domain are mainly based on a *single*-objective optimization problem aiming to minimize H_∞ or H_2 norms, i.e., their methods require the designer to set the GH_2 norm to some values in advance. Consequently, multi-objective finite-frequency SOF control for full-vehicle active suspension systems represents an important and challenging research subject; however, few attempts have been made in this direction, which has motivated our present research.

This paper presents the design procedure of a multi-objective finite-frequency H_∞/GH_2 SOF controller for active suspension systems. For the overall analysis of the performance demanding both the vehicle-ride comfort significantly related to vertical- and transversal-directional dynamics and the time-domain constraints related to the driving maneuverability, the controller development is performed based on a full-vehicle active suspension model. The proposed control strategy has the following key features:

First, it is based on explicit multi-objective optimal control to manage the trade-off between conflicting performance

requirements. In the formulated optimization problem, the H_∞ norms of the vehicle body vertical-/transversal-directional motions are adopted as the performance metric of controlled output for ride comfort enhancement; meanwhile, the time-domain constraints related to suspension deflection, road-holding ability, and actuator saturation are handled by the GH_2 performance metric. The Pareto front—the set of optimal solutions for the H_∞ norm and the GH_2 norm—is obtained by solving the multi-objective optimization problem. Therefore, the proposed strategy can give the designer the opportunity to select the optimal point efficiently.

Second, its optimal control problem is subject to finite-frequency constraints formulated based on the generalized KYP (GKYP) lemma for realizing the targeted disturbance attenuation over the specific frequency range. The improvement of overall ride comfort for full-vehicle is equivalent to minimizing the H_∞ norm for the vertical and transversal accelerations separately over their respective finite-frequency bands. The decoupled state-space models proposed in this research enable heave/pitch motion and roll motion to be handled independently and are separately exploited for the development of heave/pitch and roll motion controllers that perform optimally over their respective specific finite-frequency bands.

Third, it provides an easy-to-use design methodology of SOF controllers subject to finite-frequency constraints, which do not demand full information of all state variables, for full-car active suspension systems. Metaheuristic multi-objective optimization techniques can be used as a promising alternative to manage the control synthesis conditions formulated as non-convex BMIs in designing the SOF controller as well as to provide a direct multi-objective treatment of conflicting performance specifications in H_∞/GH_2 optimal control. Therefore, in this study, a novel multi-objective particle swarm optimization (MOPSO) algorithm is developed. This optimization mechanism efficiently explores the relevant trade-offs between the considered multiple objectives and eventually provides a set of equally valid solutions while maintaining the genuine multi-objective nature of our controller synthesis problem.

Furthermore, in a practical situation, the active suspensions should tolerate the performance loss and fluctuation due to uncertain variations in vehicle load and suspension stiffness/damping characteristics. A very reasonable assumption is that such uncertainties of suspension systems can be modeled as polytopic uncertainties. Therefore, this research handles the multi-objective finite-frequency robust H_∞/GH_2 SOF control synthesis for a full-vehicle active suspension system subject to polytopic uncertainties. The performance potential of the finite-frequency SOF H_∞/GH_2 control developed by the multi-objective metaheuristic optimizer is evaluated through simulations of the full-car active suspension model. The remainder of this paper is structured as follows. The full-vehicle active suspension model and its detailed control problems are described in Section II. Further, the decoupled state-space realization of a full-vehicle active suspension system with parameter uncertainties is presented in Section III. Then, the designing of the proposed finite-frequency SOF H_∞/GH_2 controller using the multi-objective metaheuristic optimizer is described in Section IV. Finally, simulation results illustrating the effectiveness of the proposed control synthesis method are presented in Section V, followed by concluding remarks in Section VI.

TABLE 1. Nomenclature of vehicle parameters in a full-car model ($i = 1, 2, 3, 4$).

Symbol	Model parameter	Unit
m_s	sprung mass of vehicle body	kg
m_i	vehicle unsprung mass	kg
k_{ti}	stiffness of tire	N/m
k_i	stiffness of active suspension	N/m
c_i	damping of active suspension	N·s/m
z_c	displacement of sprung mass at the geometric center	m
z_{ri}	road input to the four wheels	m
z_{ui}	displacement of unsprung masses	m
z_{si}	displacement of sprung masses	m
u_i	control effort of the actuators in the active suspension	N
θ	pitch angle of sprung mass	rad
ϕ	roll angle of sprung mass	rad
f_i	force applied on the sprung mass	N
l_f and l_r	distances from center of gravity to the front and rear axles	m
l_w	track width	m
I_x	roll axis moment of inertia	$\mathrm{kg}\cdot\mathrm{m}^2$
I_y	pitch axis moment of inertia	$\mathrm{kg}\cdot\mathrm{m}^2$

Notations: For a matrix $\boldsymbol{F}$, its transpose and complex conjugate transpose are denoted by $\boldsymbol{F}^T$ and $\boldsymbol{F}^H$. The spaces of complex and real rectangular matrices are denoted as $\mathbb{C}^{m\times n}$ and $\mathbb{R}^{m\times n}$, respectively. The symbol $\mathscr{H}_n$ is the set of $n \times n$ Hermitian matrices. An imaginary number is represented by $j = \sqrt{-1}$. The symbols $\lambda_{\max}(\boldsymbol{F})$ and $\sigma_{\max}(\boldsymbol{F})$ are the maximum eigenvalue and singular value of matrix $\boldsymbol{F}$, respectively. The symbol $\vec{0}_{m\times n}$ is the $m \times n$ null matrix.

II. FULL-CAR ACTIVE SUSPENSION SYSTEM AND PROBLEM STATEMENTS

A full-car model integrated with an active suspension system, as shown schematically in Figure 1, is considered in this research. The nomenclature of vehicle parameters shown in Figure 1 are summarized in Table 1. The active suspension between the sprung and unsprung masses at the four corners of the sprung mass comprises in series of a spring, passive damper and actuator. The vertical displacements of unsprung and sprung masses are denoted by z_{ui} and z_{si} ($i = 1, 2, 3, 4$), respectively. Moreover, the sprung mass has the heave (z_c), pitch (θ), and roll (ϕ) degrees of freedom (DOF). The tire between the unsprung mass and road is modeled as a spring, and z_{ri} denotes the vertical road disturbance under i-th tire. Note that because the damping of a tire is comparatively small, the tire-damping effect is usually omitted. Therefore, this full-car suspension model has seven DOF (7-DOF), which include the heave, pitch, and roll of the

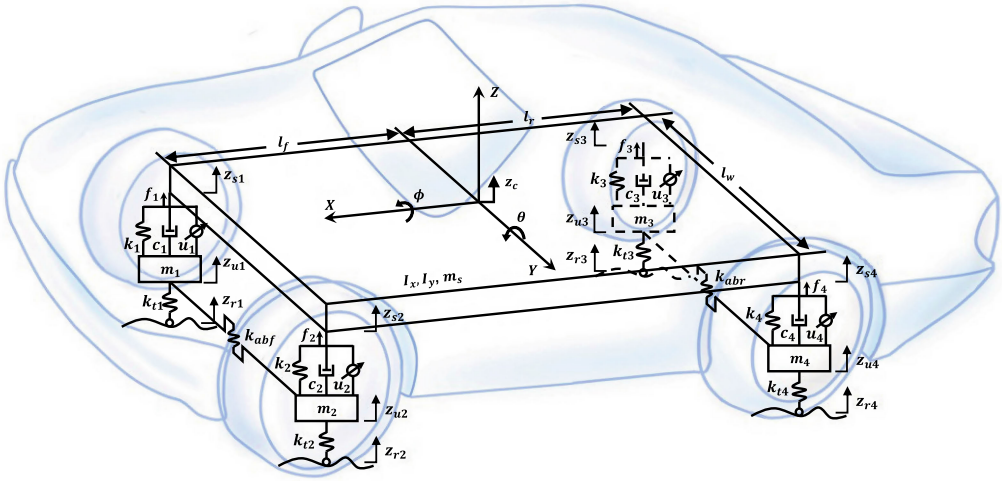

FIGURE 1. Full-car active suspension model with seven degrees of freedom.

sprung mass and vertical displacement of the four unsprung masses. Meanwhile, the antiroll bar connects right and left unsprung masses together through short lever arms linked by a torsional spring, which helps to reduce the body roll of a vehicle by resisting any uneven vertical motion between a pair of wheels. A global reference coordinate O-xyz is assumed to be at the geometric center of the sprung mass.

A. DYNAMIC EQUATIONS OF MOTION FOR A FULL-VEHICLE MODEL WITH AN ACTIVE SUSPENSION SYSTEM

The vehicle's heave motion is related to vertical translation along the z-axis, the pitch motion is related to rotational movement with respect to the y-axis, and the roll motion is related to rotational movement with respect to the x-axis. Then, the dynamic equations for a sprung mass m_s for vertical, pitch, and roll movements are formulated using Newton's second law of motion as follows:

$$m_s\ddot{z}_c = f_1 + f_2 + f_3 + f_4, \tag{1}$$
$$I_y\ddot{\theta} = -l_f(f_1 + f_2) + l_r(f_3 + f_4), \tag{2}$$
$$I_x\ddot{\phi} = \frac{l_w}{2}(-f_1 + f_2 - f_3 + f_4) - M_{abf} - M_{abr}, \tag{3}$$

where f_i $(i = 1, 2, 3, 4)$—the force applied on the sprung mass at four corners through the spring, damper, and actuator of the suspension system—is expressed as

$$f_i = -k_i(z_{si} - z_{ui}) - c_i(\dot{z}_{si} - \dot{z}_{ui}) + u_i, \tag{4}$$

and M_{abf} and M_{abr}—the torques generated by the front and rear antiroll bars, respectively—are written as [25]:

$$M_{abf} = k_{abf}\phi, \quad M_{abr} = k_{abr}\phi, \tag{5}$$

where k_{abf} and k_{abr} denote the torsional stiffness coefficients of the front and rear antiroll bars, respectively. Furthermore, the pitch and roll angles induced during the vehicle movement are assumed to be small, and such a small-angle approximation—simplifies z_{si} in (4) and M_{abf} and M_{abr} in (5)—is given as follows:

$$\begin{aligned} z_{s1} &= z_c - l_f \sin\theta - (l_w/2)\sin\phi \\ &\approx z_c - l_f\theta - (l_w/2)\phi, \end{aligned} \tag{6}$$
$$\begin{aligned} z_{s2} &= z_c - l_f \sin\theta + (l_w/2)\sin\phi \\ &\approx z_c - l_f\theta + (l_w/2)\phi, \end{aligned} \tag{7}$$
$$\begin{aligned} z_{s3} &= z_c + l_r \sin\theta - (l_w/2)\sin\phi \\ &\approx z_c + l_r\theta - (l_w/2)\phi, \end{aligned} \tag{8}$$
$$\begin{aligned} z_{s4} &= z_c + l_r \sin\theta + (l_w/2)\sin\phi \\ &\approx z_c + l_r\theta + (l_w/2)\phi, \end{aligned} \tag{9}$$

and

$$M_{abf} \approx \frac{k_{abf}}{l_w}\{(z_{s2} - z_{u2}) - (z_{s1} - z_{u1})\}, \tag{10}$$
$$M_{abr} \approx \frac{k_{abr}}{l_w}\{(z_{s4} - z_{u4}) - (z_{s3} - z_{u3})\}. \tag{11}$$

The force equilibrium in the four unsprung masses m_i $(i = 1, 2, 3, 4)$ with respect to vertical movements can be easily summarized as follows:

$$m_1\ddot{z}_{u1} = -f_1 - k_{t1}(z_{u1} - z_{r1}) - M_{abf}/l_w, \tag{12}$$
$$m_2\ddot{z}_{u2} = -f_2 - k_{t2}(z_{u2} - z_{r2}) + M_{abf}/l_w, \tag{13}$$
$$m_3\ddot{z}_{u3} = -f_3 - k_{t3}(z_{u3} - z_{r3}) - M_{abr}/l_w, \tag{14}$$
$$m_4\ddot{z}_{u4} = -f_4 - k_{t4}(z_{u4} - z_{r4}) + M_{abr}/l_w. \tag{15}$$

Because a bilaterally symmetric structure is a common feature of vehicles, some vehicle parameters can be reasonably simplified as $m_f := m_1 = m_2$, $k_f := k_1 = k_2$, $c_f := c_1 = c_2$, $k_{tf} := k_{t1} = k_{t2}$, $m_r := m_3 = m_4$, $k_r := k_3 = k_4$, $c_r := c_3 = c_4$ and $k_{tr} := k_{t3} = k_{t4}$.

B. STATEMENTS OF THE CONTROL PROBLEM IN A FULL-CAR ACTIVE SUSPENSION SYSTEM

For an active suspension system, some of the state variables of a vehicle cannot or are difficult to measure directly in a practical situation. In such a case, a high-fidelity state observer must be developed and incorporated into the control algorithm to estimate all unmeasurable states, which often causes various difficulties in realistic implementation. These facts imply that the realization of the usual state-feedback control mechanism in operating an active suspension system may be a considerably cumbersome task. From this viewpoint, to improve the usability of an active vehicle suspension, the SOF control methodology, which does not demand full information of the state variables but enjoys the simplicity of state-feedback structure, is required. However, although the state-feedback control problem can be simply solved using LMIs, the synthesis conditions of the output-feedback case are intrinsically nonconvex, resulting in BMIs, which makes finding a feasible solution set difficult. Therefore, the main objective of this research is to develop an easy-to-use design methodology of SOF controllers for the full-car active suspension system.

In designing the SOF controller for a full-vehicle active suspension system, the performance aspects concerning vehicle-ride comfort, suspension deflection limitation, road-holding performance, actuator saturation effect, and robustness against model uncertainties should be considered; they are described in detail as follows [15], [23], [26].

(a) *Vehicle-ride comfort:* The first performance requirement is related to the ride comfort of the passengers that can be effectively measured from the magnitude of vehicle-body acceleration. In this case, the H_∞ norm is usually employed to measure the ride comfort performance of the active suspension system. However, according to ISO 2631 [19], the frequency ranges in which the human body is very sensitive to vibrations differ depending on the vertical and transversal accelerations; i.e., the human body is more sensitive in the frequency range of 4–8 Hz than other frequencies in the vertical-direction motion of a vehicle, whereas the frequency range of 0.5–2 Hz is more important for enhancing ride comfort in the transversal direction. Hence, the overall ride comfort of the full-vehicle can be improved by minimizing separately the H_∞ norm for heave/pitch and roll accelerations over their respective finite-frequency bands. These finite-frequency constraints should be explicitly incorporated into the controller design procedure; accordingly, the GKYP lemma [21] is adopted to realize the targeted disturbance attenuation over the specific frequency range.

(b) *Limitation of suspension deflection:* The comfort-oriented controller for active suspension systems usually tends to require a large suspension deflection. However, there is a physical constraint that limits the suspension deflection for structural protection; hence, the controller should be able to prevent the suspension from reaching its travel limitation. Therefore, the following constraint condition on the i-th suspension deflection, $z_{si} - z_{ui}$ with $i = 1, 2, 3, 4$, should be incorporated into the controller design procedure:

$$|z_{si}(t) - z_{ui}(t)| \leq z_{sd,max}, \tag{16}$$

where $z_{sd,max}$ denotes the maximum allowed suspension deflection.

(c) *Road-holding stability requirement:* If the wheel hop is excessive, the vehicle may lose contact with the ground, which results in the loss of traction force. Therefore, the active suspension system should guarantee the road-holding requirement, which restricts the wheel hop to ensure continuous contact of the wheels with the road. Such a requirement for vehicle safety can be formulated by enforcing the dynamic tire load to not exceed the static tire load as follows:

$$k_{t1}(z_{u1}(t) - z_{r1}(t)) + k_{t2}(z_{u2}(t) - z_{r2}(t)) \leq F_f, \tag{17}$$

$$k_{t3}(z_{u3}(t) - z_{r3}(t)) + k_{t4}(z_{u4}(t) - z_{r4}(t)) \leq F_r, \tag{18}$$

where F_f and F_r are the static tire loads of the front and rear tires, respectively, which are calculated from the following formulations derived from Newton's second law of motion:

$$F_f + F_r = (m_s + m_1 + m_2 + m_3 + m_4)g, \tag{19}$$

$$F_r(l_f + l_r) = m_s g l_f + (m_3 + m_4)g(l_f + l_r), \tag{20}$$

where g denotes the gravitational constant.

(d) *Saturation effect of actuators:* As with suspension deflection limitation, the actuator saturation is also a physical constraint of the active suspension. Actuator saturation, which is very common in an actual suspension system, could be a source of performance degradation and even vehicle instability. Therefore, the controller for active suspension system should be designed to prevent saturation by constraining its peak control force to be less than a prescribed limit, u_{max}, as

$$|u_i(t)| \leq u_{max}, \quad i = 1, 2, 3, 4. \tag{21}$$

(e) *Robustness against model uncertainties:* In a practical situation, the active suspensions should maintain the required performance levels even in the presence of uncertain variations in vehicle load and suspension stiffness/damping characteristics. A very reasonable assumption would be that such uncertainties of the suspension systems can be modeled as polytopic uncertainties. Therefore, the robust

SOF control synthesis for a full-vehicle active suspension system subject to polytopic uncertainties is worth discussing.

Synthesizing the performance metrics discussed above, in this research, a finite-frequency mixed H_∞/GH_2 SOF controller based on a full-vehicle active suspension polytopic model is developed. In the design procedure, H_∞ norms of the vehicle body vertical-/transversal-direction motions are adopted as the controller output performance metric for the desirable controller; meanwhile, the hard constraints related to suspension deflection, road-holding ability, and actuator saturation are handled as the GH_2 performance metric.

III. DECOUPLED STATE-SPACE REALIZATION FOR A FULL-VEHICLE ACTIVE SUSPENSION SYSTEM

The above discussion on vehicle-ride comfort clearly shows that because of different human-body sensitivities according to the heave/pitch and roll motions, the control effort for vibration attenuation should be separately implemented considering the finite-frequency band specified for each motion. Therefore, realization of decoupled state-space models describing different vehicle motions in advance is necessary, i.e., these decoupled models enable independent handling of heave/pitch and roll motions and are separately used in developing of heave/pitch and roll motion controllers.

First, the state-space representation describing the heave–pitch motion of a full-vehicle model is derived. To reduce the expressional complexity, the state and control variables are defined as follows:

$$\begin{aligned}
z_{s,hpf} &:= z_{s1} + z_{s2} = 2z_c - 2l_f \sin\theta \approx 2z_c - 2l_f\theta,\\
z_{s,hpr} &:= z_{s3} + z_{s4} \approx 2z_c + 2l_r\theta,\\
z_{u,hpf} &:= z_{u1} + z_{u2}, \quad z_{u,hpr} := z_{u3} + z_{u4},\\
z_{r,hpf} &:= z_{r1} + z_{r2}, \quad z_{r,hpr} := z_{r3} + z_{r4},\\
z_{sd,hpf} &:= (z_{s1} - z_{u1}) + (z_{s2} - z_{u2}),\\
z_{sd,hpr} &:= (z_{s3} - z_{u3}) + (z_{s4} - z_{u4}),\\
z_{td,hpf} &:= (z_{u1} - z_{r1}) + (z_{u2} - z_{r2}),\\
z_{td,hpr} &:= (z_{u3} - z_{r3}) + (z_{u4} - z_{r4}),
\end{aligned}$$

and

$$u_{hpf} := u_1 + u_2, \quad u_{hpr} := u_3 + u_4,$$

where $z_{s,hpf}$ and $z_{s,hpr}$ are easily confirmed from (6)-(7) and (8)-(9), respectively. The suspension and tire deflections are denoted by $z_{sd,i}$ and $z_{td,i}$ $(i = 1, 2, 3, 4)$ as $z_{sd,i} := z_{si} - z_{ui}$ and $z_{td,i} := z_{ui} - z_{ri}$, respectively. Defining the state vector $\boldsymbol{x}_{hp} = [\dot{z}_{s,hpf},\ \dot{z}_{s,hpr},\ z_{sd,hpf},\ z_{sd,hpr},\ \dot{z}_{u,hpf},\ \dot{z}_{u,hpr},\ z_{td,hpf},\ z_{td,hpr}]^T \in \mathbb{R}^8$, disturbance vector $\boldsymbol{w}_{hp} = [\dot{z}_{r,hpf},\ \dot{z}_{r,hpr}]^T \in \mathbb{R}^2$, and control input vector $\boldsymbol{u}_{hp} = [u_{hpf},\ u_{hpr}]^T \in \mathbb{R}^2$, the state-space realization corresponding to the full-vehicle heave–pitch motion can be obtained as

$$\dot{\boldsymbol{x}}_{hp}(t) = A_{hp}\boldsymbol{x}_{hp}(t) + B_{w,hp}\boldsymbol{w}_{hp}(t) + B_{u,hp}\boldsymbol{u}_{hp}(t), \tag{22}$$

where $A_{hp} \in \mathbb{R}^{8\times8}$, $B_{w,hp} \in \mathbb{R}^{8\times2}$, and $B_{u,hp} \in \mathbb{R}^{8\times2}$ are

$$A_{hp} = \begin{bmatrix} [A_{hp}]_{11} & [A_{hp}]_{12} \\ [A_{hp}]_{21} & [A_{hp}]_{22} \end{bmatrix}, \tag{23}$$

$$[A_{hp}]_{11} = \begin{bmatrix} -2a_1c_f & -2a_2c_r & -2a_1k_f & -2a_2k_r \\ -2a_2c_f & -2a_3c_r & -2a_2k_f & -2a_3k_r \\ 1 & 0 & 0 & 0 \\ 0 & 1 & 0 & 0 \end{bmatrix},$$

$$[A_{hp}]_{12} = \begin{bmatrix} 2a_1c_f & 2a_2c_r & 0 & 0 \\ 2a_2c_f & 2a_3c_r & 0 & 0 \\ -1 & 0 & 0 & 0 \\ 0 & -1 & 0 & 0 \end{bmatrix},$$

$$[A_{hp}]_{21} = \begin{bmatrix} \frac{c_f}{m_f} & 0 & \frac{k_f}{m_f} & 0 \\ 0 & \frac{c_r}{m_r} & 0 & \frac{k_r}{m_r} \\ 0 & 0 & 0 & 0 \\ 0 & 0 & 0 & 0 \end{bmatrix},$$

$$[A_{hp}]_{22} = \begin{bmatrix} -\frac{c_f}{m_f} & 0 & -\frac{k_{tf}}{m_f} & 0 \\ 0 & -\frac{c_r}{m_r} & 0 & -\frac{k_{tr}}{m_r} \\ 1 & 0 & 0 & 0 \\ 0 & 1 & 0 & 0 \end{bmatrix},$$

$$B_{w,hp} = \begin{bmatrix} 0 & 0 & 0 & 0 & 0 & 0 & -1 & 0 \\ 0 & 0 & 0 & 0 & 0 & 0 & 0 & -1 \end{bmatrix}^T, \tag{24}$$

$$B_{u,hp} = \begin{bmatrix} 2a_1 & 2a_2 & 0 & 0 & -\frac{1}{m_f} & 0 & 0 & 0 \\ 2a_2 & 2a_3 & 0 & 0 & 0 & -\frac{1}{m_r} & 0 & 0 \end{bmatrix}^T \tag{25}$$

with $a_1 := \frac{1}{m_s} + \frac{l_f^2}{I_y}$, $a_2 := \frac{1}{m_s} - \frac{l_f l_r}{I_y}$ and $a_3 := \frac{1}{m_s} + \frac{l_r^2}{I_y}$. The detailed derivation of the above state-space form can be found in Appendix A.

Further, to specify the performance requirements related to the heave–pitch motion of an active vehicle suspension system, the performance output vectors—$\boldsymbol{z}_{1,hp} \in \mathbb{R}^2$ and $\boldsymbol{z}_{2,hp} \in \mathbb{R}^6$—are defined as follows:

$$\boldsymbol{z}_{1,hp} = \left[q_1\ddot{z}_c\ q_2\ddot{\theta}\right]^T, \tag{26}$$

$$\begin{aligned}
\boldsymbol{z}_{2,hp} &= \left[[\boldsymbol{z}_{2,hp}]_{11}\ [\boldsymbol{z}_{2,hp}]_{12}\ [\boldsymbol{z}_{2,hp}]_{13}\right]^T,\\
[\boldsymbol{z}_{2,hp}]_{11} &= \left[\frac{z_{sd,hpf}}{2z_{sd,max}}\ \frac{z_{sd,hpr}}{2z_{sd,max}}\right],\\
[\boldsymbol{z}_{2,hp}]_{12} &= \left[\frac{k_{tf}z_{td,hpf}}{F_f}\ \frac{k_{tr}z_{td,hpr}}{F_r}\right],\\
[\boldsymbol{z}_{2,hp}]_{13} &= \left[\frac{u_{hpf}}{2u_{max}}\ \frac{u_{hpr}}{2u_{max}}\right],
\end{aligned} \tag{27}$$

where q_1 and q_2 are just coefficients for adjusting the weights between heave and pitch accelerations during the H_∞ norm-related optimization procedure. For the clarity of presentation, q_1 is chosen as 1 and q_2 is defined as $q_2 := q_1\sqrt{l_f l_r}$ [24], [27]. Then, the performance output equations corresponding to the heave–pitch motion of a full-vehicle model are developed from (1), (2), (4), (16), (17), (18), and (21) as follows:

$$\boldsymbol{z}_{1,hp}(t) = C_{1,hp}\boldsymbol{x}_{hp}(t) + D_{w1,hp}\boldsymbol{w}_{hp}(t) + D_{u1,hp}\boldsymbol{u}_{hp}(t), \tag{28}$$

$$\boldsymbol{z}_{2,hp}(t) = C_{2,hp}\boldsymbol{x}_{hp}(t) + D_{w2,hp}\boldsymbol{w}_{hp}(t) + D_{u2,hp}\boldsymbol{u}_{hp}(t), \tag{29}$$

where $C_{1,hp} \in \mathbb{R}^{2\times 8}$, $D_{u1,hp} \in \mathbb{R}^{2\times 2}$, $C_{2,hp} \in \mathbb{R}^{6\times 8}$, and $D_{u2,hp} \in \mathbb{R}^{6\times 2}$ are given as follows:

$$C_{1,hp} = \begin{bmatrix} q_1 & 0 \\ 0 & q_2 \end{bmatrix} \begin{bmatrix} -c_f/m_s & l_f c_f/I_y \\ -c_r/m_s & -l_r c_r/I_y \\ -k_f/m_s & l_f k_f/I_y \\ -k_r/m_s & -l_r k_r/I_y \\ c_f/m_s & -l_f c_f/I_y \\ c_r/m_s & l_r c_r/I_y \\ 0 & 0 \\ 0 & 0 \end{bmatrix}^T, \tag{30}$$

$$D_{u1,hp} = \begin{bmatrix} q_1 & 0 \\ 0 & q_2 \end{bmatrix} \begin{bmatrix} 1/m_s & 1/m_s \\ -l_f/I_y & l_r/I_y \end{bmatrix}, \tag{31}$$

$$C_{2,hp} = \begin{bmatrix} 0 & 0 & \frac{1}{2z_{sd,max}} & 0 & 0 & 0 & 0 & 0 \\ 0 & 0 & 0 & \frac{1}{2z_{sd,max}} & 0 & 0 & 0 & 0 \\ 0 & 0 & 0 & 0 & 0 & 0 & \frac{k_{tf}}{F_f} & 0 \\ 0 & 0 & 0 & 0 & 0 & 0 & 0 & \frac{k_{tr}}{F_r} \\ 0 & 0 & 0 & 0 & 0 & 0 & 0 & 0 \\ 0 & 0 & 0 & 0 & 0 & 0 & 0 & 0 \end{bmatrix}, \tag{32}$$

$$D_{u2,hp} = \begin{bmatrix} 0 & 0 & 0 & 0 & \frac{1}{2u_{max}} & 0 \\ 0 & 0 & 0 & 0 & 0 & \frac{1}{2u_{max}} \end{bmatrix}^T, \tag{33}$$

and $D_{w1,hp}$ and $D_{w2,hp}$ are null matrices with appropriate dimensions [28]. The derivations of these equations are given in Appendix B. Noting the following two facts is important: (i) the performance output vector $z_{1,hp}$ is introduced for considering the vehicle-ride comfort performance and will be used later for optimizing the H_∞ norm-related objective function over the finite frequency range of 4–8 Hz; (ii) the other vector $z_{2,hp}$, which has been normalized, is selected with the aim of handling suspension deflection, road-holding ability and actuator saturation, which will be achieved via the optimization of the GH_2 norm-related objective function.

Next, the state and controlled output equations of the state-space form, which describe the roll motion of a full-vehicle model, are developed. The state and control variables related to the roll motion are chosen as

$$\begin{aligned} z_{s,rf} &:= z_{s2} - z_{s1}, \quad z_{s,rr} := z_{s4} - z_{s3}, \\ z_{u,rf} &:= z_{u2} - z_{u1}, \quad z_{u,rr} := z_{u4} - z_{u3}, \\ z_{r,rf} &:= z_{r2} - z_{r1}, \quad z_{r,rr} := z_{r4} - z_{r3}, \end{aligned}$$

and

$$u_{rf} := -u_1 + u_2, \quad u_{rr} := -u_3 + u_4.$$

Then, the state, disturbance, and input vectors are defined as $\boldsymbol{x}_r = [z_{u,rf},\ z_{u,rr},\ \phi,\ \dot{z}_{u,rf},\ \dot{z}_{u,rr},\ \dot{\phi}]^T \in \mathbb{R}^6$, $\boldsymbol{w}_r = [z_{r,rf},\ z_{r,rr}]^T \in \mathbb{R}^2$, and $\boldsymbol{u}_r = [u_{rf},\ u_{rr}]^T \in \mathbb{R}^2$, respectively. The state-space form for the full-vehicle roll motion is derived from the dynamic equations in (3), (4), and (10)-(15) with $z_{s2} - z_{s1} \approx l_w\phi$ and $z_{s4} - z_{s3} \approx l_w\phi$ as follows:

$$\dot{\boldsymbol{x}}_r(t) = A_r\boldsymbol{x}_r(t) + B_{w,r}\boldsymbol{w}_r(t) + B_{u,r}\boldsymbol{u}_r(t), \tag{34}$$

where $A_r \in \mathbb{R}^{6\times 6}$, $B_{w,r} \in \mathbb{R}^{6\times 2}$, and $B_{u,r} \in \mathbb{R}^{6\times 2}$ are given as follows:

$$A_r = \begin{bmatrix} \vec{0}_{3\times 2} & \vec{0}_{3\times 1} & I_3 \\ [A_r]_{21} & [A_r]_{22} & [A_r]_{23} \end{bmatrix}, \tag{35}$$

$$[A_r]_{21} = \begin{bmatrix} -\frac{k_{tf}+k_f}{m_f} & -\frac{2k_{abf}}{m_f l_w^2} & 0 \\ 0 & -\frac{k_{tr}+k_r}{m_r} & -\frac{2k_{abr}}{m_r l_w^2} \\ \frac{k_f l_w}{2I_x} + \frac{k_{abf}}{I_x l_w} & \frac{k_r l_w}{2I_x} + \frac{k_{abr}}{I_x l_w} & \end{bmatrix},$$

$$[A_r]_{22} = \begin{bmatrix} \frac{k_f l_w}{m_f} + \frac{2k_{abf}}{m_f l_w} \\ \frac{k_r l_w}{m_r} + \frac{2k_{abr}}{m_r l_w} \\ -\frac{k_f l_w^2 + k_r l_w^2}{2I_x} - \frac{k_{abf}+k_{abr}}{I_x} \end{bmatrix},$$

$$[A_r]_{23} = \begin{bmatrix} -\frac{c_f}{m_f} & 0 & \frac{c_f l_w}{m_f} \\ 0 & -\frac{c_r}{m_r} & \frac{c_r l_w}{m_r} \\ \frac{c_f l_w}{2I_x} & \frac{c_r l_w}{2I_x} & -\frac{c_f l_w^2 + c_r l_w^2}{2I_x} \end{bmatrix},$$

$$B_{w,r} = \begin{bmatrix} 0 & 0 & 0 & \frac{k_{tf}}{m_f} & 0 & 0 \\ 0 & 0 & 0 & 0 & \frac{k_{tr}}{m_r} & 0 \end{bmatrix}^T, \tag{36}$$

$$B_{u,r} = \begin{bmatrix} 0 & 0 & 0 & -\frac{1}{m_f} & 0 & \frac{l_w}{2I_x} \\ 0 & 0 & 0 & 0 & -\frac{1}{m_r} & \frac{l_w}{2I_x} \end{bmatrix}^T. \tag{37}$$

The derivation of the above state equation is presented in Appendix C.

Then, the performance output equations for the full-vehicle roll motion are developed. Defining $z_{sd,rf} := -(z_{s1} - z_{u1}) + (z_{s2} - z_{u2}) = -z_{sd,1} + z_{sd,2}$ and $z_{sd,rr} := -(z_{s3} - z_{u3}) + (z_{s4} - z_{u4}) = -z_{sd,3} + z_{sd,4}$, the controlled output vectors—$z_{1,r} \in \mathbb{R}$ and $z_{2,r} \in \mathbb{R}^4$—are defined as follows:

$$z_{1,r} = \left[\ddot{\phi}\right],\ z_{2,r} = \left[\frac{z_{sd,rf}}{2z_{sd,max}},\ \frac{z_{sd,rr}}{2z_{sd,max}},\ \frac{u_{rf}}{2u_{max}},\ \frac{u_{rr}}{2u_{max}}\right]^T. \tag{38}$$

Similar to the case of heave–pitch motion, (i) the controlled output vector $z_{1,r}$ is used to evaluate the roll-directional ride comfort through the optimization of the H_∞ norm-related objective function over the finite frequency range of 0.5–2 Hz, and (ii) the other vector $z_{2,r}$ is selected for the GH_2 optimization related to suspension deflection, road-holding ability and actuator saturation. Then, the controlled output equations can be obtained from (3), (4), (10), (11), (16), and (21) as follows:

$$z_{1,r}(t) = C_{1,r}\boldsymbol{x}_r(t) + D_{w1,r}\boldsymbol{w}_r(t) + D_{u1,r}\boldsymbol{u}_r(t), \tag{39}$$

$$z_{2,r}(t) = C_{2,r}\boldsymbol{x}_r(t) + D_{w2,r}\boldsymbol{w}_r(t) + D_{u2,r}\boldsymbol{u}_r(t), \tag{40}$$

where $C_{1,r} \in \mathbb{R}^{1\times 6}$, $D_{u1,r} \in \mathbb{R}^{1\times 2}$, $C_{2,r} \in \mathbb{R}^{4\times 6}$, and $D_{u2,r} \in \mathbb{R}^{4\times 2}$ are given as follows:

$$C_{1,r} = \begin{bmatrix} \frac{k_f l_w}{2I_x} + \frac{k_{abf}}{I_x l_w} \\ \frac{k_r l_w}{2I_x} + \frac{k_{abr}}{I_x l_w} \\ -\frac{k_f l_w^2 + k_r l_w^2 + 2k_{abf} + 2k_{abr}}{2I_x} \\ \frac{c_f l_w}{2I_x} \\ \frac{c_r l_w}{2I_x} \\ -\frac{c_f l_w^2 + c_r l_w^2}{2I_x} \end{bmatrix}^T, \tag{41}$$

$$D_{u1,r} = \begin{bmatrix} \frac{l_w}{2I_x} & \frac{l_w}{2I_x} \end{bmatrix}, \tag{42}$$

$$C_{2,r} = \begin{bmatrix} -\frac{1}{2z_{sd,max}} & 0 & \frac{l_w}{2z_{sd,max}} & 0\,0\,0 \\ 0 & -\frac{1}{2z_{sd,max}} & \frac{l_w}{2z_{sd,max}} & 0\,0\,0 \\ 0 & 0 & 0 & 0\,0\,0 \\ 0 & 0 & 0 & 0\,0\,0 \end{bmatrix}, \tag{43}$$

$$D_{u2,r} = \begin{bmatrix} 0\,0 & \frac{1}{2u_{max}} & 0 \\ 0\,0 & 0 & \frac{1}{2u_{max}} \end{bmatrix}^T, \tag{44}$$

and $D_{w1,r}$ and $D_{w2,r}$ are null matrices with appropriate dimensions [28]. The derivation of the above state equations can be found in Appendix D.

The SOF control problem for a full-vehicle active suspension system is then considered. Because the decoupled state-space models describing heave/pitch and roll motions are developed, two controls—$\boldsymbol{u}_{hp}(t)$ in (22) and $\boldsymbol{u}_r(t)$ in (34)—can be developed independently, i.e., our SOF control problem is to find two types of constant matrix gains, $K_{hp} \in \mathbb{R}^{2\times4}$ and $K_r \in \mathbb{R}^{2\times3}$, in the following control laws:

$$\boldsymbol{u}_{hp}(t) = K_{hp}\boldsymbol{y}_{hp}(t), \quad \boldsymbol{u}_r(t) = K_r\boldsymbol{y}_r(t), \tag{45}$$

where $\boldsymbol{y}_{hp} \in \mathbb{R}^4$, the measured output vector related to the heave/pitch motion, is chosen as

$$\begin{aligned} \boldsymbol{y}_{hp}(t) &= \begin{bmatrix} \dot{z}_{s,hpf}(t) \\ \dot{z}_{s,hpr}(t) \\ z_{sd,hpf}(t) \\ z_{sd,hpr}(t) \end{bmatrix} = C_{hp}\boldsymbol{x}_{hp}(t) \\ &= \underbrace{\begin{bmatrix} 1\,0\,0\,0\,0\,0\,0\,0 \\ 0\,1\,0\,0\,0\,0\,0\,0 \\ 0\,0\,1\,0\,0\,0\,0\,0 \\ 0\,0\,0\,1\,0\,0\,0\,0 \end{bmatrix}}_{C_{hp}} \boldsymbol{x}_{hp}(t) \end{aligned} \tag{46}$$

and $\boldsymbol{y}_r \in \mathbb{R}^3$, the measured output vector related to the roll motion, is

$$\begin{aligned} \boldsymbol{y}_r(t) &= \begin{bmatrix} z_{sd,rf}(t) \\ z_{sd,rr}(t) \\ \dot{\phi}(t) \end{bmatrix} = C_r\boldsymbol{x}_r(t) \\ &= \underbrace{\begin{bmatrix} -1 & 0 & l_w & 0\,0\,0 \\ 0 & -1 & l_w & 0\,0\,0 \\ 0 & 0 & 0 & 0\,0\,1 \end{bmatrix}}_{C_r} \boldsymbol{x}_r(t) \end{aligned} \tag{47}$$

Compared with the state-feedback counterparts, the SOF control policies use limited types of signals, which are on-line measurable in realistic situations. For example, tire deflection cannot be measured or is not simple to measure in practice, whereas suspension deflection and suspension travel velocity are known to be easily obtainable [29]. Therefore, the measurable output vector $\boldsymbol{y} \in \mathbb{R}^8$ is assumed to be as follows:

$$\boldsymbol{y} = \begin{bmatrix} \dot{z}_{s1} & \dot{z}_{s2} & \dot{z}_{s3} & \dot{z}_{s4} & z_{sd1} & z_{sd2} & z_{sd3} & z_{sd4} \end{bmatrix}^T, \tag{48}$$

where $\dot{z}_{si}$ $(i = 1, 2, 3, 4)$ is the absolute linear velocity of the sprung mass at the four suspensions and $z_{sd,i}(= z_{si} - z_{ui})$ denotes the suspension deflection. The important problem in this case is to find a method for extracting the information on $\boldsymbol{y}_{hp}$ in (46) and $\boldsymbol{y}_r$ in (47) from $\boldsymbol{y}$ in (48), which is simply achieved by using the transformation matrix T_1 as

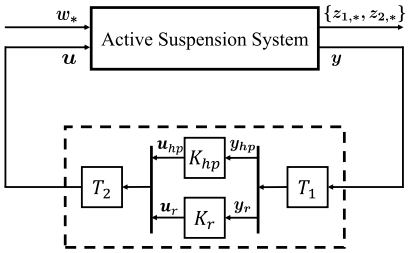

FIGURE 2. Closed-loop control configuration for a full-car active suspension system.

$$\begin{aligned} \begin{bmatrix} \boldsymbol{y}_{hp} \\ \boldsymbol{y}_r \end{bmatrix} &= \begin{bmatrix} \dot{z}_{s,hpf} \\ \dot{z}_{s,hpr} \\ z_{sd,hpf} \\ z_{sd,hpr} \\ z_{sd,rf} \\ z_{sd,rr} \\ \dot{\phi} \end{bmatrix} = T_1\boldsymbol{y} \\ &= \underbrace{\begin{bmatrix} 1 & 1 & 0\,0 & 0 & 0 & 0 & 0 \\ 0 & 0 & 1\,1 & 0 & 0 & 0 & 0 \\ 0 & 0 & 0\,0 & 1 & 1 & 0 & 0 \\ 0 & 0 & 0\,0 & 0 & 0 & 1 & 1 \\ 0 & 0 & 0\,0 & -1 & 1 & 0 & 0 \\ 0 & 0 & 0\,0 & 0 & 0 & -1 & 1 \\ -1/l_w & 1/l_w & 0\,0 & 0 & 0 & 0 & 0 \end{bmatrix}}_{T_1} \begin{bmatrix} \dot{z}_{s1} \\ \dot{z}_{s2} \\ \dot{z}_{s3} \\ \dot{z}_{s4} \\ z_{sd,1} \\ z_{sd,2} \\ z_{sd,3} \\ z_{sd,4} \end{bmatrix} \end{aligned} \tag{49}$$

where $\dot{\phi} = -(1/l_w)\dot{z}_{s1} + (1/l_w)\dot{z}_{s2}$ can be easily confirmed from (6)-(7). Moreover, the control force u_i $(i = 1, 2, 3, 4)$ is necessary for actuating the suspension system as (4), but the control laws (45) developed later produce $\boldsymbol{u}_{hp} = [u_{hpf},\ u_{hpr}]^T$ and $\boldsymbol{u}_r = [u_{rf},\ u_{rr}]^T$. However, such control forces, u_i, can be easily calculated from four control variables, namely, u_{hpf}, u_{hpr}, u_{rf}, and u_{rr}, as follows:

$$\begin{bmatrix} u_1 \\ u_2 \\ u_3 \\ u_4 \end{bmatrix} = \underbrace{\begin{bmatrix} 1 & 1 & 0 & 0 \\ 0 & 0 & 1 & 1 \\ -1 & 1 & 0 & 0 \\ 0 & 0 & -1 & 1 \end{bmatrix}^{-1}}_{T_2} \begin{bmatrix} u_{hpf} \\ u_{hpr} \\ u_{rf} \\ u_{rr} \end{bmatrix} = T_2 \begin{bmatrix} \boldsymbol{u}_{hp} \\ \boldsymbol{u}_r \end{bmatrix}. \tag{50}$$

Based on the above observation, the overall closed-loop configuration of a SOF control for a full-car active suspension system can be depicted as shown in Figure 2.

Finally, the modeling technique to achieve robustness against model uncertainties mentioned in the previous section is considered. In this research, to capture the parametric uncertainties of the nominal models (i.e., (22), (28), and (29) for heave–pitch motion and (34), (39), and (40) for roll motion), polytopic parameter uncertainties were

employed [30]. Then, the model considering uncertainties for the aforementioned full-vehicle dynamics can be further described by

$$\begin{cases} \dot{\boldsymbol{x}}_*(t) = A_*(\lambda)\boldsymbol{x}_*(t) + B_{w,*}(\lambda)\boldsymbol{w}_*(t) + B_{u,*}(\lambda)\boldsymbol{u}_*(t), \\ \boldsymbol{z}_{1,*}(t) = C_{1,*}(\lambda)\boldsymbol{x}_*(t) + D_{w1,*}(\lambda)\boldsymbol{w}_*(t) + D_{u1,*}(\lambda)\boldsymbol{u}_*(t), \\ \boldsymbol{z}_{2,*}(t) = C_{2,*}(\lambda)\boldsymbol{x}_*(t) + D_{w2,*}(\lambda)\boldsymbol{w}_*(t) + D_{u2,*}(\lambda)\boldsymbol{u}_*(t), \\ \boldsymbol{y}_*(t) = C_*\boldsymbol{x}_*(t), \end{cases} \tag{51}$$

where the symbol '$*$' refers to 'hp' for the heave/pitch-related state-space equations or 'r' for the roll-related state-space equations. Here, the matrices $A_*(\lambda)$, $B_{w,*}(\lambda)$, $B_{u,*}(\lambda)$, $C_{1,*}(\lambda)$, $D_{w1,*}(\lambda)$, $D_{u1,*}(\lambda)$, $C_{2,*}(\lambda)$, $D_{w2,*}(\lambda)$, and $D_{u2,*}(\lambda)$ are constrained within the convex bounded polyhedral domain Ψ given by

$$\Psi \triangleq \left\{ \Phi(\lambda) \;\middle|\; \Phi(\lambda) = \sum_{i=1}^{n_v} \lambda_i \Phi_i; \;\; \sum_{i=1}^{n_v} \lambda_i = 1, \;\; \lambda_i \geq 1 \right\} \tag{52}$$

where Φ_i denotes the vertices of the polytope as

$$\Phi_i \triangleq (A_*^i, \; B_{w,*}^i, \; B_{u,*}^i, \; C_{1,*}^i, \; D_{w1,*}^i, \; D_{u1,*}^i, \; C_{2,*}^i, \; D_{w2,*}^i, \; D_{u2,*}^i), \tag{53}$$

n_v is the number of vertices, and $\boldsymbol{\lambda} = \{\lambda_1, \; \lambda_2, \cdots, \lambda_{n_v}\}^T$ is the polytope coordinate vector. Therefore, by substituting the SOF controls in (45) into the polytopic model of the form in (51), the closed-loop system can be rewritten as

$$\begin{cases} \dot{\boldsymbol{x}}_*(t) = \mathcal{A}_*(\lambda)\boldsymbol{x}_*(t) + B_{w,*}(\lambda)\boldsymbol{w}_*(t), \\ \boldsymbol{z}_{1,*}(t) = \mathcal{C}_{1,*}(\lambda)\boldsymbol{x}_*(t) + D_{w1,*}(\lambda)\boldsymbol{w}_*(t), \\ \boldsymbol{z}_{2,*}(t) = \mathcal{C}_{2,*}(\lambda)\boldsymbol{x}_*(t) + D_{w2,*}(\lambda)\boldsymbol{w}_*(t), \end{cases} \tag{54}$$

where $\mathcal{A}_*(\lambda) := (A_*(\lambda) + B_{u,*}(\lambda)K_*C_*)$, $\mathcal{C}_{1,*}(\lambda) := (C_{1,*}(\lambda) + D_{u1,*}(\lambda)K_*C_*)$, and $\mathcal{C}_{2,*}(\lambda) := (C_{2,*}(\lambda) + D_{u2,*}(\lambda)K_*C_*)$.

IV. FINITE-FREQUENCY SOF H_∞/GH_2 CONTROL SYNTHESIS VIA MULTI-OBJECTIVE METAHEURISTIC OPTIMIZER

In the previous section, two nominal state-space models were first realized from dynamic equations of motion for a full-vehicle model with the active suspension system presented in Section II-A: (22), (28), (29), and (46) for describing the heave–pitch motion and (34), (39), (40), and (47) for the roll motion. Then, to handle uncertain variations in vehicle load and suspension stiffness/damping characteristics, those state-space formulations were extended to polytopic-type uncertain systems in the form of (51). It should be noted that the performance outputs $(\boldsymbol{z}_{1,hp}, \boldsymbol{z}_{1,r})$ are used for respectively measuring heave/pitch motion-related vehicle-ride comfort performance over the 4–8-Hz finite frequency range and roll-motion-related vehicle-ride comfort performance over the 0.5–2-Hz frequency range. Meanwhile, the other performance outputs $(\boldsymbol{z}_{2,hp}, \boldsymbol{z}_{2,r})$ are for considering other performance aspects such as suspension deflection, road-holding ability and actuator saturation. In summary, the finite-frequency H_∞/GH_2 control problem for a full-vehicle active suspension system involves the development of the SOF controls in (45), which are capable of asymptotically stabilizing the closed-loop systems in (54) and simultaneously considering both $(\boldsymbol{z}_{1,hp}, \boldsymbol{z}_{1,r})$-related finite-frequency H_∞ performance indices and $(\boldsymbol{z}_{2,hp}, \boldsymbol{z}_{2,r})$-related GH_2 performance indices.

A. FINITE-FREQUENCY SOF H_∞/GH_2 CONTROLLER DESIGN

The strategy for handling the vehicle-ride comfort performance in the controller design procedure is first considered. The finite-frequency (from $\bar{\omega}_L$ to $\bar{\omega}_H$) H_∞ performance of transfer function from the road disturbance $\boldsymbol{w}_*$ to the performance output $\boldsymbol{z}_{1,*}$ can be improved by minimizing $\gamma_\infty (> 0)$ such that $\sup_{\bar{\omega}_L \leq \omega \leq \bar{\omega}_H} \sigma_{\max}\left(\frac{\boldsymbol{z}_{1,*}(j\omega)}{\boldsymbol{w}_*(j\omega)}\right) < \gamma_\infty$. The following GKYP lemma provides the equivalence between a frequency-domain inequality and an LMI to be solved over a finite frequency range [21]. It is adopted for evaluating and reducing the aforementioned H_∞ norm from $\boldsymbol{w}_*$ to $\boldsymbol{z}_{1,*}$ over a specific frequency band in which the human body is more sensitive to vibrations.

Lemma 1 (Finite-Frequency H_∞ Performance): Consider the closed-loop system (54) with polytopic uncertainty (52)-(53). Suppose that a set of auxiliary matrices $(\mathcal{A}_*^i, \; B_{w,*}^i, \; \mathcal{C}_{1,*}^i, \; D_{w1,*}^i)$ where $i = 1, 2, \cdots, n_v$, and n_x, the dimension of state vector $\boldsymbol{x}_*$, are given. For a given scalar $\gamma_\infty > 0$, the finite-frequency H_∞ performance $\sup_{\bar{\omega}_L \leq \omega \leq \bar{\omega}_H} \sigma_{\max}\left(\frac{\boldsymbol{z}_{1,*}(j\omega)}{\boldsymbol{w}_*(j\omega)}\right) < \gamma_\infty$ holds if and only if there exist $P^i \in \mathcal{H}_{n_x}$, $Q^i \in \mathcal{H}_{n_x}$, and $G \in \mathbb{C}^{n_x \times n_x}$ such that $Q^i \succ 0$ and the matrix inequality

$$\begin{bmatrix} -Q^i & P^i + j\omega_c Q^i - G^H & 0 & 0 \\ * & -\bar{\omega}_L\bar{\omega}_H Q^i + G\mathcal{A}_*^i + \mathcal{A}_*^{iT} G^H & GB_{w,*}^i & \mathcal{C}_{1,*}^{iT} \\ * & * & -\gamma_\infty^2 I & D_{w1,*}^{iT} \\ * & * & * & -I \end{bmatrix} \prec 0, \tag{55}$$

where $\omega_c = (\bar{\omega}_L + \bar{\omega}_H)/2$ with $(\bar{\omega}_L, \bar{\omega}_H) = (4 \times 2\pi, 8 \times 2\pi)$ rad/s for heave/pitch motion and $(\bar{\omega}_L, \bar{\omega}_H) = (0.5 \times 2\pi, 2 \times 2\pi)$ rad/s for roll motion, is feasible.

The proof of the above lemma can be easily derived from [31]; therefore, it is omitted here. Note that the H_∞ norm is introduced as the measure of ride comfort performance because the H_∞ norm of a linear time-invariant system equals the energy-to-energy gain and its value actually gives an upper bound on the root-mean-square (RMS) gain [23].

Furthermore, because the GH_2 norm is defined as an energy-to-peak norm (or L_2–L_∞-induced norm), the GH_2 performance from the road disturbance $\boldsymbol{w}_*$ to the performance output $\boldsymbol{z}_{2,*}$ is introduced to constrain $\boldsymbol{z}_{2,*}$, which is related to suspension deflection, road-holding ability and actuator saturation, within a given bound. The following lemma states the LMI condition such that the GH_2 norm becomes less than a positive scalar γ_2, which guarantees that the performance output L_∞ norm does not exceed a predefined maximum.

Lemma 2 (GH_2 Performance): Consider the closed-loop system (54) with polytopic uncertainty (52)-(53). Suppose that a set of auxiliary matrices $(\mathcal{A}^i_*, B^i_{w,*}, \mathcal{C}^i_{2,*}, D^i_{w2,*})$, $i = 1, 2, \cdots, n_v$ is given. Then, for a given scalar $\gamma_2 > 0$, the GH_2 performance $\frac{\|z_{2,*}(t)\|_\infty}{\|\boldsymbol{w}_*(t)\|_2} < \gamma_2$ holds if and only if there exist symmetric matrix variables $X^i = X^{i^T} \succ 0$ such that

$$\begin{bmatrix} X^i & X^i\mathcal{C}^{i^T}_{2,*} \\ \mathcal{C}^i_{2,*}X^i & \gamma_2^2 I \end{bmatrix} \succ 0, \tag{56}$$

$$\begin{bmatrix} X^i\mathcal{A}^{i^T}_* + \mathcal{A}^i_* X^i & B^i_{w,*} \\ B^{i^T}_{w,*} & -I \end{bmatrix} \prec 0, \tag{57}$$

are feasible.

Proof: Consider the closed-loop polytopic system (54). For a given positive scalar γ_2, the system (54) is internally stable and $\frac{\|z_2(t)\|^2_\infty}{\|w(t)\|^2_2} < \gamma_2^2$ holds if and only if $D^i_{w2,*}$ is the null matrix and $Y^i \succ 0$, which satisfies the following conditions, exists [32]:

$$\lambda_{\max}(\mathcal{C}^i_{2,*}Y^i\mathcal{C}^{i^T}_{2,*}) < \gamma_2^2, \tag{58}$$

$$\mathcal{A}^i_* Y^i + Y^i\mathcal{A}^{i^T}_* + B^i_{w,*}B^{i^T}_{w,*} \prec 0. \tag{59}$$

The inequality condition (58) can be rewritten in a matrix inequality form as:

$$\lambda_{\max}(\mathcal{C}^i_{2,*}Y^i\mathcal{C}^{i^T}_{2,*}) < \gamma_2^2 \iff \mathcal{C}^i_{2,*}Y^i\mathcal{C}^{i^T}_{2,*} \prec \gamma_2^2 I. \tag{60}$$

Then, the Schur complement with respect to $\mathcal{C}^i_{2,*}Y^i\mathcal{C}^{i^T}_{2,*}$ yields

$$\begin{bmatrix} (Y^i)^{-1} & \mathcal{C}^{i^T}_{2,*} \\ \mathcal{C}^i_{2,*} & \gamma_2^2 I \end{bmatrix} \succ 0. \tag{61}$$

The congruence transformation by diagonal matrix $\begin{bmatrix} X^i & 0 \\ 0 & I \end{bmatrix}$ with $X^i := (Y^i)^{-1}$ leads to the matrix inequality (56). Further, the matrix inequality (57) can be derived by applying a Schur complement with respect to $B^i_{w,*}B^{i^T}_{w,*}$ for the matrix inequality (59). ∎

The above two lemmas provide the result that the control gain matrices K_{hp} and K_r in (45) satisfying the LMI constraints presented in those lemmas guarantee the finite-frequency H_∞ performance and GH_2 performance for all nonzero $\boldsymbol{w}(t) \in L_2[0, \infty)$. Therefore, the optimal control gain matrices can be obtained by minimizing the positive constants γ_∞ and γ_2. However, the simultaneous minimization of both γ_∞ and γ_2 is difficult because finite-frequency H_∞ and GH_2 performances are highly conflicting, e.g., enhancing the vehicle-ride comfort usually requires a larger suspension deflection. It means that a performance requirement cannot be met without detriment to the other requirement. Therefore, our multiple-demand SOF controller design task for (45) should be treated as a multi-objective programming problem as

$$\begin{aligned} &\text{minimize } [\gamma_\infty, \gamma_2], \\ &\text{subject to (55), (56), (57) with } Q^i \succ 0 \text{ and } X^i \succ 0. \end{aligned} \tag{62}$$

This mathematical formulation appears to allow various multi-objective optimization methodologies to be readily applied for finding a set of feasible optimal gain matrices $\{K_{hp}, K_r\}$ with different trade-offs. However, it is very important to note that the above multi-objective optimization problem for designing finite-frequency SOF H_∞/GH_2 controllers is, in fact, clearly involving a problem of BMIs, which is an NP-hard problem and thus has been scarcely tractable numerically until the present day. This can be easily confirmed from the fact that (55) and (57) involve some products of unknown matrices, e.g., $GB^i_{u,*}K_*C^i_*$, which results from $G\mathcal{A}^i_*$ in (55) and involves two unknown matrices G and K_*, and $B^i_{u,*}K_*C_*X^i$, which results from $\mathcal{A}^i_*X^i$ in (57) and involves two unknown matrices X^i and K_*.

For managing this difficulty in solving the multi-objective design problem, metaheuristic multi-objective optimization techniques represent as a promising alternative that can provide a direct multi-objective treatment of performance specifications formulated using BMIs in the controller synthesis procedure. Therefore, the MOPSO algorithm is developed in this study. This optimization mechanism efficiently explores the relevant trade-offs between the considered multiple objectives and eventually provides a set of equally valid solutions, known as Pareto-optimal solutions, while maintaining the genuine multi-objective nature of our controller synthesis problem.

B. MULTI-OBJECTIVE PARTICLE SWARM OPTIMIZATION ALGORITHM

Let a design variable vector be denoted by $\vec{\boldsymbol{x}} = [x_1, x_2, \cdots, x_{dm}]^T$. The optimal vector of $\vec{\boldsymbol{x}}$ is found by minimizing a vector $\vec{\mathcal{L}}(\vec{\boldsymbol{x}})$ of n_f objective functions, $\mathcal{L}_\ell(\vec{\boldsymbol{x}})$ (with $\ell = 1, 2, \cdots, n_f$), which are in conflict with one another. Then, the general multi-objective optimization problem is stated as

$$\begin{aligned} &\text{minimize } \vec{\mathcal{L}}(\vec{\boldsymbol{x}}) = [\mathcal{L}_1(\vec{\boldsymbol{x}}), \mathcal{L}_2(\vec{\boldsymbol{x}}), \cdots, \mathcal{L}_{n_f}(\vec{\boldsymbol{x}})]^T \\ &\text{subject to } \vec{\boldsymbol{x}} \in \mathcal{S}, \end{aligned} \tag{63}$$

where $\mathcal{S}$ denotes the space of feasible solutions where all constraint functions are satisfied. In what follows, Pareto dominance, Pareto optimality, and Pareto-optimal set are briefly described (refer to [33] for details). Consider two design variable vectors $\vec{\boldsymbol{x}}_\alpha$ and $\vec{\boldsymbol{x}}_\beta$. A vector $\vec{\mathcal{L}}(\vec{\boldsymbol{x}}_\alpha) = [\mathcal{L}_1(\vec{\boldsymbol{x}}_\alpha), \cdots, \mathcal{L}_{n_f}(\vec{\boldsymbol{x}}_\alpha)]^T$ is said to dominate $\vec{\mathcal{L}}(\vec{\boldsymbol{x}}_\beta) = [\mathcal{L}_1(\vec{\boldsymbol{x}}_\beta), \cdots, \mathcal{L}_{n_f}(\vec{\boldsymbol{x}}_\beta)]^T$ if and only if $\mathcal{L}_\ell(\vec{\boldsymbol{x}}_\alpha) \le \mathcal{L}_\ell(\vec{\boldsymbol{x}}_\beta)\ \forall \ell = \{1, \cdots, n_f\}$ and $\mathcal{L}_\ell(\vec{\boldsymbol{x}}_\alpha) < \mathcal{L}_\ell(\vec{\boldsymbol{x}}_\beta)$ for $\exists i = \{1, \cdots, n_f\}$. A design variable vector $\vec{\boldsymbol{x}} \in \mathcal{S}$ is Pareto-optimal (i.e., non-dominated solution) if no objective function $\mathcal{L}_\ell(\vec{\boldsymbol{x}})$ can be improved without worsening the rest, which refers to that there is not any design variable vector that dominates the Pareto-optimal. A set containing every possible optimal design vector $\vec{\boldsymbol{x}} \in \mathcal{S}$ is a Pareto-optimal set. The boundary defined by the set of all points mapped from the Pareto-optimal set is called the Pareto-optimal front.

A particle swarm optimization (PSO) algorithm is a well-known swarm-based stochastic algorithm, and its canonical mechanism is formulated as follows [34], [35]. A set of n_p particles is considered a population, where each particle j has a position vector (i.e., design variable vector) $\vec{\boldsymbol{x}}_j^k = [x_{j,1}^k, x_{j,2}^k, \cdots, x_{j,dm}^k]^T \in \mathbb{R}^{dm}, j = 1, 2, \cdots, n_p$ and velocity vector $\vec{\boldsymbol{v}}_j^k = [v_{j,1}^k, v_{j,2}^k, \cdots, v_{j,dm}^k]^T \in \mathbb{R}^{dm}$ with dm design variables at the generation k. In the next generation $k+1$, the velocity and position vectors of the jth particle are updated as follows:

$$\vec{\boldsymbol{v}}_j^{k+1} = c_0\vec{\boldsymbol{v}}_j^k + c_1\boldsymbol{r}_{1,j}^k(\vec{\boldsymbol{x}}_{pbest,j}^k - \vec{\boldsymbol{x}}_j^k) + c_2\boldsymbol{r}_{2,j}^k(\vec{\boldsymbol{x}}_{gbest}^k - \vec{\boldsymbol{x}}_j^k), \quad (64)$$

$$\vec{\boldsymbol{x}}_j^{k+1} = \vec{\boldsymbol{x}}_j^k + \vec{\boldsymbol{v}}_j^{k+1}, \quad (65)$$

where c_0 is the inertia factor, c_1 is the cognitive scaling factor, c_2 is the social scaling factor, and $\boldsymbol{r}_{1,j}^k \in \mathbb{R}^{d_m \times d_m}$ and $\boldsymbol{r}_{2,j}^k \in \mathbb{R}^{d_m \times d_m}$ are diagonal matrices, with their elements being random numbers distributed uniformly in $[0, 1]$. Note that matrices $\boldsymbol{r}_{1,j}^k$ and $\boldsymbol{r}_{2,j}^k$ are generated at each iteration for each particle independently. In (64), $\vec{\boldsymbol{x}}_{pbest,j}^k$ denotes the best position among positions that the jth particle has experienced until the k-th generation, and $\vec{\boldsymbol{x}}_{gbest,j}^k$ denotes the position of the global-best particle found over the entire swarm, which guides the particles to move toward the optimal solution, i.e.

$$\vec{\boldsymbol{x}}_{pbest,j}^k := \arg \min_{\vec{\boldsymbol{x}} \in \{\vec{\boldsymbol{x}}_j^i | i=1,\cdots,k\}} \mathcal{L}(\vec{\boldsymbol{x}}), \quad (66)$$

$$\vec{\boldsymbol{x}}_{gbest}^k := \arg \min_{\vec{\boldsymbol{x}} \in \{\vec{\boldsymbol{x}}_j^k | j=1,\cdots,n_p\}} \mathcal{L}(\vec{\boldsymbol{x}}). \quad (67)$$

In a single-objective PSO algorithm, the computational procedure can be briefly summarized as follows. All particles are randomly generated within the search space in the initial iteration of swarm evolution. Then, the swarm particles are evaluated using a given single-objective function for their own fitness values as well as global optimum fitness, which provides $\vec{\boldsymbol{x}}_{pbest,j}^k$ and $\vec{\boldsymbol{x}}_{gbest}^k$. Following (64) and (65), each particle determines its next movement throughout the problem's solution space, ultimately based on both its personal historical pathway information as $(\vec{\boldsymbol{x}}_{pbest,j}^k - \vec{\boldsymbol{x}}_j^k)$ and the temporary best trajectory of the entire swarm as $(\vec{\boldsymbol{x}}_{gbest}^k - \vec{\boldsymbol{x}}_j^k)$. Once all the particles have their respective movements updated at the current step, the next iteration of the search procedure starts, and eventually, the entire swarm gradually converges toward the optimum of the single-objective function.

Contrary to the above single-objective optimization case, a deliberate decision of a sole global-best position $\vec{\boldsymbol{x}}_{gbest}^k$ is very important when the PSO technique is applied to multi-objective optimization problems. In multi-objective cases, the Pareto-optimal set containing the candidates of real optimal solutions is constructed at each iteration. Furthermore, in such a Pareto-optimal set, an element (i.e., the local-best guide) that is used as $\vec{\boldsymbol{x}}_{gbest}^k$ should be selected for each iteration to apply the PSO update rule (64). In our optimizer for solving the multi-objective optimization problem of finite-frequency SOF H_∞/GH_2 control synthesis, the global-best selection via roulette-wheel for areas separated by several hypercubes is adopted to obtain the local-best guide $\vec{\boldsymbol{x}}_{gbest}^k$ [36]. Moreover, the proposed multi-objective PSO algorithm exploits the mutation method with a quantum-principle-based infusion mechanism [37], [38] to improve the exploration ability of the swarm. The multi-objective quantum-behaved PSO procedure comprises the following steps:

Step 1: Set iteration $k = 0$ and the design parameters of the PSO algorithm such as n_p (population size), n_r (repository size), *maxgen* (maximum number of generations), $\{c_0, c_1, c_2\}$ (PSO hyperparameters), β (quantum-infusion hyperparameter), and $\{\vec{\boldsymbol{x}}_{\min}, \vec{\boldsymbol{x}}_{\max}\} (\in \mathbb{R}^{dm})$ (lower and upper boundaries of $\vec{\boldsymbol{x}}$). Initialize the repository of Pareto optimals *REP* as the null set ($REP = \{\}$). The initialization of position and velocity vectors of each particle in the swarm is realized as

$$\vec{\boldsymbol{x}}_j^0 = \vec{\boldsymbol{x}}_{\min} + \text{diag}[\text{rand}(1, dm)] \times (\vec{\boldsymbol{x}}_{\max} - \vec{\boldsymbol{x}}_{\min}), \quad (68)$$

$$\vec{\boldsymbol{v}}_j^0 = \vec{\boldsymbol{0}}, \quad (69)$$

where diag[rand$(1, dm)$] denotes a diagonal matrix whose elements are random numbers distributed uniformly in $[0, 1]$, and $j = 1, 2, \cdots, n_p$.

Step 2: Evaluate fitness values $\mathcal{L}_i(\vec{\boldsymbol{x}}_j^k)$, where $i = 1, 2, \cdots, n_f$, of all particles.

Step 3: Check whether $\vec{\boldsymbol{x}}_j^k$ dominates $\vec{\boldsymbol{x}}_\ell^k$ for $\ell \neq j$. If such a $\vec{\boldsymbol{x}}_j^k$ is not dominated by any of the others, store it in the repository *REP*. In addition, check the dominant relationship between $\vec{\boldsymbol{x}}_j^k$ and $\vec{\boldsymbol{x}}_{pbest,j}^{k-1}$. Then, if $\vec{\boldsymbol{x}}_j^k$ dominates $\vec{\boldsymbol{x}}_{pbest,j}^{k-1}$, update $\vec{\boldsymbol{x}}_{pbest,j}^k$ as $\vec{\boldsymbol{x}}_{pbest,j}^k \leftarrow \vec{\boldsymbol{x}}_j^k$, else if $\vec{\boldsymbol{x}}_j^k$ is not dominated by $\vec{\boldsymbol{x}}_{pbest,j}^{k-1}$, update $\vec{\boldsymbol{x}}_{pbest,j}^k$ as $\vec{\boldsymbol{x}}_{pbest,j}^k \leftarrow \vec{\boldsymbol{x}}_j^k$ with 50% probability. Otherwise, $\vec{\boldsymbol{x}}_{pbest,j}^k$ remains unchanged.

Step 4: Generate the hypercubes of the space comprising Pareto optimals of *REP*. Then, assign the roulette fitness values to each Pareto-optimal particle by calculating the number of Pareto optimals in a hypercube. Subsequently, select $\vec{\boldsymbol{x}}_{gbest}^k$ through roulette-wheel selection.

Step 5: Update the velocity and position vectors, $\vec{\boldsymbol{v}}_j^{k+1}$ and $\vec{\boldsymbol{x}}_j^{k+1}$, by following the update laws in (64)-(65).

Step 6: Randomly select some particles (e.g., one-third of the particles) in the swarm. Then, mutate those particles via the quantum-principle-based infusion mechanism to explore an extensive region as

$$\begin{aligned}\vec{\boldsymbol{x}}_j^{k+1} \leftarrow\ & \boldsymbol{r}_{3,j}^k \vec{\boldsymbol{x}}_{pbest,j}^k + (I - \boldsymbol{r}_{3,j}^k)\vec{\boldsymbol{x}}_{gbest,j}^k \\ & + (I - 2 \times \text{round}(\boldsymbol{r}_{4,j}^k))\beta \\ & \times |\vec{\boldsymbol{x}}_{mbest,j}^k - \vec{\boldsymbol{x}}_j^{k+1}| \ln(1/\boldsymbol{r}_{5,j}^k) \end{aligned} \quad (70)$$

where $\{\boldsymbol{r}_{3,j}^k, \boldsymbol{r}_{4,j}^k, \boldsymbol{r}_{5,j}^k\} \in \mathbb{R}^{d_m \times d_m}$ are diagonal matrices, with their elements being random numbers distributed uniformly in $[0, 1]$; β denotes the creativity coefficient introduced for adjusting

the convergence speed of the particle; round($\boldsymbol{r}^k_{4,j}$) denotes a matrix in which each element of $\boldsymbol{r}^k_{4,j}$ is rounded to the nearest integer; and $\vec{\boldsymbol{x}}^k_{mbest,j} := \frac{1}{n_p}[\sum_{i=1}^{n_p} x_{i,1}, \sum_{i=1}^{n_p} x_{i,2} \cdots, \sum_{i=1}^{n_p} x_{i,dm}]^T$ denotes the mean position of the population. In our application, the size of a mutated particle is set to decrease with every iteration.

Step 7: If the termination criterion is satisfied (e.g., k becomes equal to a given *maxgen*), return the Pareto-optimal solutions in *REP*. Otherwise, go to Step 2.

The above procedure is only applicable to multi-objective optimization problems without constraints, i.e., this procedure involves no technique for handling constraints such as the boundary constraints of optimization variables. To make it capable of dealing with constraints, the aforementioned optimization procedure is extended using the promising constraint-handling technique in metaheuristic algorithms [39]. Let the multi-objective constrained optimization problem be given as follows: Minimize $\vec{\mathcal{F}}(\vec{\boldsymbol{x}}) = [\mathcal{F}_1(\vec{\boldsymbol{x}}), \mathcal{F}_2(\vec{\boldsymbol{x}}), \cdots, \mathcal{F}_{n_f}(\vec{\boldsymbol{x}})]^T$ subject to $g_\ell(\vec{\boldsymbol{x}}) \le 0$, where $\ell = 1, 2, \cdots, n_g$. The boundary constraint functions can be defined as $g_\ell(\vec{\boldsymbol{x}}) := \vec{\boldsymbol{x}} - \vec{\boldsymbol{x}}_{\max}$ and $g_\ell(\vec{\boldsymbol{x}}) := \vec{\boldsymbol{x}}_{\min} - \vec{\boldsymbol{x}}$. In this case, the evaluation of fitness values required in Step 2 is performed as follows: for $i = 1, 2, \cdots, n_f$ and $j = 1, 2, \cdots, n_p$,

$$\mathcal{L}_i(\vec{\boldsymbol{x}}^k_j) := \begin{cases} g_{\max}(\vec{\boldsymbol{x}}^k_j), & \text{if } g_{\max}(\vec{\boldsymbol{x}}^k_j) > 0, \\ \arctan[\mathcal{F}_i(\vec{\boldsymbol{x}}^k_j)] - \dfrac{\pi}{2}, & \text{otherwise,} \end{cases} \tag{71}$$

where $g_{\max}(\vec{\boldsymbol{x}}^k_j) := \arg\max_{g_\ell(\vec{\boldsymbol{x}}^k_j)}[g_1(\vec{\boldsymbol{x}}^k_j), \cdots, g_{n_g}(\vec{\boldsymbol{x}}^k_j)]$ and $\arctan[\cdot]$ denotes the arctangent function. Note that $\mathcal{L}_i(\vec{\boldsymbol{x}}^k_j) > 0$ holds if $g_\ell(\vec{\boldsymbol{x}}^k_j) > 0$ holds for $\exists \ell = \{1, 2, \cdots, n_g\}$. Thus, if $\vec{\boldsymbol{x}}^k_j$ is an infeasible solution (i.e., at least one constraint is violated), the modified fitness value $\mathcal{L}_i(\vec{\boldsymbol{x}}^k_j)$ is a positive number, while if $\vec{\boldsymbol{x}}^k_j$ is feasible, $\mathcal{L}_i(\vec{\boldsymbol{x}}^k_j)$ has a negative value because $(\arctan[\mathcal{F}_i(\vec{\boldsymbol{x}}^k_j)] - \frac{\pi}{2}) < 0$ for any $\vec{\boldsymbol{x}}^k_j$. Therefore, the modified formulation in (71) enforces that a feasible solution always takes a smaller negative fitness value than the positive value of an infeasible solution, which continuously encourages a particle belonging to an infeasible search space to move into a feasible space. Further, as $(\arctan[\cdot] - \frac{\pi}{2})$ is a continuous strictly monotonic function of $\mathcal{F}_i(\vec{\boldsymbol{x}}^k_j)$, the property $\mathcal{L}_i(\vec{\boldsymbol{x}}^k_\alpha) \le \mathcal{L}_i(\vec{\boldsymbol{x}}^k_\beta)$ holds for $\mathcal{F}_i(\vec{\boldsymbol{x}}^k_\alpha) \le \mathcal{F}_i(\vec{\boldsymbol{x}}^k_\beta)$, where $\vec{\boldsymbol{x}}^k_\alpha$ and $\vec{\boldsymbol{x}}^k_\beta$ are feasible solutions.

C. APPLICATION OF MULTI-OBJECTIVE QUANTUM-BEHAVED PSO ALGORITHM FOR FINITE-FREQUENCY SOF H_∞/GH_2 CONTROL SYNTHESIS

This section presents the method to find control gain matrices K_{hp} and K_r in (45) by solving the multi-objective control synthesis problem (62) using the multi-objective quantum-behaved PSO algorithm. The introduced PSO algorithm eventually provides the Pareto-optimal set containing all possible Pareto optimals, which are equally valid alternative solutions from the viewpoint of multiple objectives and eventually provide a set of multiple candidates K_*.

Let $K_*^{(i,j)}$ denote the element at the intersection of the i-th row and j-th column of the K_* matrix, where $i \in \{1, 2\}$, $j \in \{1, 2, 3, 4\}$ for K_{hp} or $j \in \{1, 2, 3\}$ for K_r. Then, the control gain matrix $K_{hp} \in \mathbb{R}^{2\times 4}$ can be reshaped into a design variable vector $\vec{\boldsymbol{x}} \in \mathbb{R}^8$ as $\vec{\boldsymbol{x}} = [K_{hp}^{(1,1)}, K_{hp}^{(1,2)}, K_{hp}^{(1,3)}, K_{hp}^{(1,4)}, K_{hp}^{(2,1)}, K_{hp}^{(2,2)}, K_{hp}^{(2,3)}, K_{hp}^{(2,4)}]^T$. The control gain matrix $K_r \in \mathbb{R}^{2\times 3}$ can also be reshaped into a vector $\vec{\boldsymbol{x}} \in \mathbb{R}^6$ in a similar way. Then, two conflicting objective functions $[\mathcal{L}_1(\vec{\boldsymbol{x}}), \mathcal{L}_2(\vec{\boldsymbol{x}})]$ are defined as follows:

(i) $\mathcal{L}_1(\vec{\boldsymbol{x}}) := \gamma_\infty$, where γ_∞ is the upper boundary of the H_∞ norm of the transfer function from $\boldsymbol{w}_*$ to $\boldsymbol{z}_{1,*}$ as $\gamma_\infty > \sup_{\bar{\omega}_L \le \omega \le \bar{\omega}_H} \sigma_{\max}\left(\frac{z_{1,*}(j\omega)}{w_*(j\omega)}\right)$;

(ii) $\mathcal{L}_2(\vec{\boldsymbol{x}}) := \gamma_2$, where γ_2 is the upper boundary of the GH_2 norm of the transfer function from $\boldsymbol{w}_*$ to $\boldsymbol{z}_{2,*}$ as $\gamma_2 > \frac{\|z_{2,*}(t)\|_\infty}{\|w_*(t)\|_2}$.

Note that as K_* is generated from $\vec{\boldsymbol{x}}$, both $\gamma_\infty (=: \mathcal{L}_1(\vec{\boldsymbol{x}}))$ and $\gamma_2 (=: \mathcal{L}_2(\vec{\boldsymbol{x}}))$ depend on K_*. In what follows, a brief overall description of how the multi-objective quantum-behaved PSO scheme described in Section IV-B operates for solving the multi-objective control synthesis problem formulated in (62) is given. Once the position vector $\vec{\boldsymbol{x}}$ and velocity vector $\vec{\boldsymbol{v}}$ of each particle are initialized in Step 1, Step 2 requires the evaluation of fitness values $\mathcal{L}_1(\vec{\boldsymbol{x}}) (:= \gamma_\infty)$ and $\mathcal{L}_2(\vec{\boldsymbol{x}}) (:= \gamma_2)$ by solving the given control synthesis problem (62). It can be easily inferred in this case that the BMI constraints, (55) and (57), are reduced to LMI constraints because K_* are fixed by the selected position vector $\vec{\boldsymbol{x}}$ (e.g., $GB^i_{u,*}K_*C^i_*$, which comes from GA^i_* in (55), to involve only one unknown matrix G). It means that our multi-objective control synthesis problem with BMI constraints is transformed by the PSO technique into a problem with LMI constraints. However, although calculating $\mathcal{L}_1(\vec{\boldsymbol{x}})$ and $\mathcal{L}_2(\vec{\boldsymbol{x}})$ may appear straightforward, some additional complex procedures for evaluating these fitness functions are necessary. The first one is to check whether the closed-loop system in the form of (54) with the considered K_* (i.e., $\vec{\boldsymbol{x}}$) is Lyapunov stable. The second one is to check the feasibility of $\vec{\boldsymbol{x}}$ for LMI constraints in (55), (56), and (57) and then handle the infeasible vector $\vec{\boldsymbol{x}}$-related problems within the PSO structure. In our optimization technique, the modified function (71) for fitness value evaluation contributes to the easy separation of feasible and infeasible solutions. If the considered $\vec{\boldsymbol{x}}$ is infeasible for a certain constraint function, the value of that function is replaced by a considerably large positive number to clarify the infeasibility of $\vec{\boldsymbol{x}}$ during the optimization process. The detailed pseudocode for evaluating fitness values is presented as Algorithm 1. Once $\mathcal{L}_1(\vec{\boldsymbol{x}})$ and $\mathcal{L}_2(\vec{\boldsymbol{x}})$ are evaluated by following the procedure of Algorithm 1, the following remaining steps are consecutively performed: (Step 3) examining the dominance of $\vec{\boldsymbol{x}}$ to update $\vec{\boldsymbol{x}}_{pbest,j}$; (Step 4) selecting $\vec{\boldsymbol{x}}_{gbest}$ via the roulette-wheel selection technique; (Step 5) updating the velocity and position vectors;

Algorithm 1 Evaluation of Fitness Values at the k-Th PSO Iteration

Begin
for $i = 1 : n_p$
  $g_1(\vec{x}_i^k) := \max([(x_{i,1}^k - x_{\max,1}), \cdots, (x_{i,dm}^k - x_{\max,dm})])$
  $g_2(\vec{x}_i^k) := \max([(x_{\min,1} - x_{i,1}^k), \cdots, (x_{\min,dm} - x_{i,dm}^k)])$
  $K_* = \text{reshape}(\vec{x}_i^k, (n_u, n_y))$ where $K_* \in \mathbb{R}^{n_u \times n_y}$

  (Begin LMI solver-programming for checking the Lyapunov stability)
  Define variables(P_0, μ)
  condition$_0 := P_0 \succ 0$
  for $j = 1$ to n_v
    condition$_j := \mathcal{A}_*^{j^T} P_0 + P_0 \mathcal{A}_*^j \preceq \mu I$
  end for
  obj1 := μ
  Solve LMI1([condition$_0$, $\cdots$, condition$_{n_v}$], obj1)
  (End of LMI solver-programming)

  if LMI1 is infeasible
    $g_3(\vec{x}_i^k) := \epsilon (\gg 0)$
  else if $\mu \geq 0$ (stability condition is not satisfied) and LMI1 is feasible
    $g_3(\vec{x}_i^k) := \mu \times \eta$ satisfying $\eta \gg 0$ and $\mu \cdot \eta < \epsilon$
  else if $\mu < 0$ (stability condition is satisfied) and LMI1 is feasible

    (Begin LMI solver-programming related to H_∞ norm)
    Define variables (G, P^j, Q^j, γ_∞)
    condition$_{H_\infty,0} := \gamma_\infty > 0$
    for $j = 1$ to n_v
      condition$_{H_\infty,j} := [Q^j \succ 0,$ inequality (55)$]$
    end for
    obj2 := γ_∞
    Solve LMI2([condition$_{H_\infty,0}$, $\cdots$, condition$_{H_\infty,n_v}$], obj2)
    if LMI2 is feasible
      $\mathcal{F}_1(\vec{x}_i^k) :=$ value(obj2)
      $g_4(\vec{x}_i^k) := \delta (\ll 0)$
    else
      $g_4(\vec{x}_i^k) := \delta (\gg 0)$
    end if
    (End of LMI solver-programming)

    (Begin LMI solver-programming related to GH_2 norm)
    Define variables(X^j, γ_2)
    condition$_{GH_2,0} := \gamma_2 > 0$
    for $j = 1$ to n_v
      condition$_{GH_2,j} := [X^j \succ 0,$ inequalities (56), (57)$]$
    end for
    obj3 := γ_2
    Solve LMI3([condition$_{GH_2,0}$, $\cdots$, condition$_{GH_2,n_v}$, obj3)
    if LMI3 is feasible
      $\mathcal{F}_2(\vec{x}_i^k) :=$ value(obj3)
      $g_5(\vec{x}_i^k) := \rho (\ll 0)$
    else
      $g_5(\vec{x}_i^k) := \rho (\gg 0)$
    end if
    (End of LMI solver-programming)

    $g_3(\vec{x}_i^k) := \max(g_4(\vec{x}_i^k), g_5(\vec{x}_i^k))$
  end if

  (Evaluation of the multi-objective fitness values)
  $g_{\max}(\vec{x}_i^k) := \max([g_1(\vec{x}_i^k), g_2(\vec{x}_i^k), g_3(\vec{x}_i^k)])$
  if $g_{\max}(\vec{x}_i^k) > 0$
    $\mathcal{L}_1(\vec{x}_i^k) \leftarrow g_{\max}(\vec{x}_i^k)$
    $\mathcal{L}_2(\vec{x}_i^k) \leftarrow g_{\max}(\vec{x}_i^k)$
  else
    $\mathcal{L}_1(\vec{x}_i^k) \leftarrow \arctan(\mathcal{F}_1(\vec{x}_i^k)) - \frac{\pi}{2}$
    $\mathcal{L}_2(\vec{x}_i^k) \leftarrow \arctan(\mathcal{F}_2(\vec{x}_i^k)) - \frac{\pi}{2}$
  end if
end for

TABLE 2. Nominal model parameters of the full-car active suspension model [18].

Parameter	Value	Parameter	Value
m_s	1,550 kg	k_f, k_r	18,000 N/m
m_f	40 kg	m_r	40 kg
k_{tf}	220,000 N/m	k_{tr}	220,000 N/m
c_f	1,400 N·s/m	c_r	1,400 N·s/m
k_{abf}	40,107 N·m/rad	k_{abr}	34,377 N·m/rad
l_f	1.5 m	l_r	1.8 m
I_x	660 kg·m^2	I_y	2,080 kg·m^2
$z_{sd,\max}$	0.1 m	$u_{\max}$	6,000 N
l_w	2 m		

TABLE 3. Model parameter variation in the case of four operating conditions.

Parameter	Operating condition 1	Operating condition 2	Operating condition 3	Operating condition 4
m_s (kg)	1,240	1,240	1,860	1,860
k_f, k_r (N/m)	14,400	21,600	14,400	21,600
c_f, c_r (N·s/m)	1,120	1,120	1,680	1,680

(Step 6) mutating a particle via the quantum-principle-based infusion mechanism.

V. SIMULATION RESULTS AND DISCUSSION

The performance potential of the finite-frequency SOF H_∞/GH_2 control developed by the multi-objective meta-heuristic optimizer is evaluated through simulations of the full-car active suspension model shown in Figure 1. The nominal model parameters, listed in Table 2, were taken from Jing et al. [18]. In our simulation results, the variations in k_f, k_r, c_f, and c_r were assumed to represent important parameter uncertainties. Then, under the assumptions of $1240 \leq m_s \leq 1860$, $14400 \leq k_f = k_r \leq 21600$, and $1120 \leq c_f = c_r \leq 1680$, such parameter uncertainties generated the polytopic model with 8 vertices, which was used for the finite-frequency SOF H_∞/GH_2 controller design. Table 3 presents four operating conditions, which correspond to some of the vertices of the polytopic model, with different sets of $\{m_s, k_f = k_r, c_f = c_r\}$. The robustness of the developed controller against parameter variations will be examined in detail for these operating conditions. Further, the following design parameters for the proposed multi-objective quantum-behaved PSO algorithm were used in the optimization procedure: n_p (population size) $= 100$; n_r (repository size) $= 150$; *maxgen* (maximum number of generations) $= 1000$; $\{c_0, c_1, c_2\}$ (PSO hyperparameters) $= \{0.7298, 1.4692, 1.4962\}$; β (quantum-infusion hyperparameter) $= 0.5 - 1.0$ (linearly increasing as the number of iterations increases); the parameter search space was limited in $[-5, 5] \times 10^5$. The PSO algorithm was coded in MATLAB R2022a with YALMIP toolbox for interfacing the external solver of LMIs and MOSEK toolbox as the LMI solver.

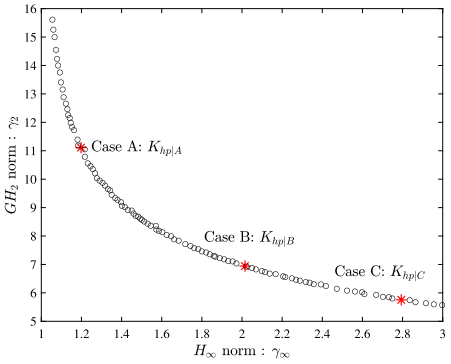

(a) Pareto front of every possible optimal controller (K_{hp}) for heave–pitch motion

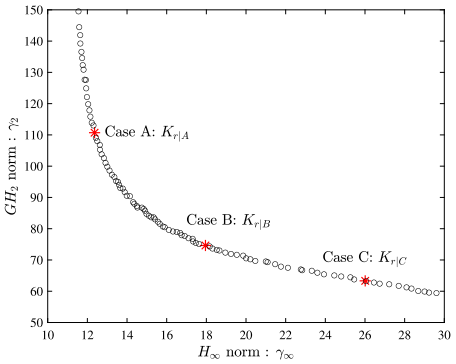

(b) Pareto front of every possible optimal controller (K_r) for roll motion

FIGURE 3. Pareto-optimal fronts of $\{\gamma_\infty, \gamma_2\}$ obtained using the multi-objective quantum-behaved PSO algorithm.

The multi-objective constrained optimization problem (62) for designing the finite-frequency SOF H_∞/GH_2 controllers in the forms of (45) was solved by following the procedure described in Section IV-C with the proposed multi-objective quantum-behaved PSO algorithm presented in Section IV-B. The obtained Pareto-optimal fronts are shown in Figure 3. Figure 3(a) presents the Pareto front of every possible K_{hp} for controlling the full-vehicle's heave/pitch motion, and Figure 3(b) presents the Pareto front of K_r for the roll motion control. The H_∞ performance γ_∞ in (62) was evaluated over the frequency ranges of 4–8 Hz for heave/pitch motion and 0.5–2 Hz for roll motion of the full-vehicle active suspension system. To verify different trade-offs in its performance, H_∞ performance related to ride comfort and GH_2 performance related to suspension deflection, road-holding ability and actuator saturation, the different sets of optimal gain matrices $\{K_{hp}, K_r\}$ were examined. The sets of control gain matrices corresponding to the three points (Cases A, B, and C) selected from the Pareto-optimal front as depicted in Figure 3 are respectively as follows:

$$\begin{cases} K_{hp|A} = \begin{bmatrix} -461.28 & 97.77 & -418.52 & 54.08 \\ 100.20 & -453.71 & 180.51 & -417.35 \end{bmatrix} \times 10^3, \\ K_{r|A} = \begin{bmatrix} -37.56 & 50.93 & -32.51 \\ 73.67 & -21.63 & -8.84 \end{bmatrix} \times 10^3, \end{cases} \tag{72}$$

$$\begin{cases} K_{hp|B} = \begin{bmatrix} -276.77 & -39.64 & -500 & -123.96 \\ 49.07 & -199.99 & 218.01 & -500 \end{bmatrix} \times 10^3, \\ K_{r|B} = \begin{bmatrix} -29.28 & 47.75 & -15.93 \\ 57.66 & -23.85 & -4.36 \end{bmatrix} \times 10^3, \end{cases} \tag{73}$$

$$\begin{cases} K_{hp|C} = \begin{bmatrix} -171.48 & -23.11 & -489.96 & -123.37 \\ 89.04 & -125.10 & 411.36 & -500 \end{bmatrix} \times 10^3, \\ K_{r|C} = \begin{bmatrix} -14.01 & 11.78 & -14.92 \\ 16.13 & -7.20 & -9.91 \end{bmatrix} \times 10^3. \end{cases} \tag{74}$$

Figures 4(a), 4(b) and 4(c) display the closed-loop frequency response curves of heave, pitch, and roll accelerations, respectively, of the sprung mass for the different SOF H_∞/GH_2 controllers after selection of the above sets of control gain matrices. As expected from the Pareto-optimal front in Figure 3, the figures show that the full-vehicle active suspension system controlled by the SOF controller with $\{K_{hp|A}, K_{r|A}\}$ yields the smallest magnitudes of the heave–pitch accelerations in the frequency ranges of 4–8 Hz and the roll acceleration in the range of 0.5–2 Hz compared with the active suspension systems with $\{K_{hp|B}, K_{r|B}\}$ and $\{K_{hp|C}, K_{r|C}\}$. This implies that the SOF H_∞/GH_2 controller embedded with $\{K_{hp|A}, K_{r|A}\}$ can effectively promote the overall ride-comfort experience of automotive vehicle passengers, i.e., the heave/pitch motion-related vehicle-ride comfort performance over the 4–8-Hz finite frequency range and the roll motion-related ride comfort performance over 0.5–2-Hz frequency range. However, the closed-loop controlled suspension system with $\{K_{hp|A}, K_{r|A}\}$ yields a relatively large GH_2-norm value compared to other cases as shown in Figure 3. This implies that the controllers (45) using $\{K_{hp|A}, K_{r|A}\}$ would be expected to cause a deterioration in performance from the viewpoint of suspension deflection, road-holding ability, and actuator saturation, which is clearly verified in the following time-domain performance analyses of the full-vehicle active suspension system.

To clarify the performance difference among the selected optimal control gain matrices $\{K_{hp|A}, K_{r|A}\}$, $\{K_{hp|B}, K_{r|B}\}$, and $\{K_{hp|C}, K_{r|C}\}$ with respect to the vehicle-ride quality and the suspension constraints in the time domain, the successive excitation of bump and random roads was assumed to be applied to our full-vehicle active suspension system. Such a road profile is generated by combining the bump signal [40] and random vibration signal generated by the displacement power spectral density (PSD) [41], which represents the combination of common and dangerous road-surface irregularities. The road displacement profile and its rate of change applied to the front-right wheel are formulated as follows:

$$z_{r1}(t) = \begin{cases} \dfrac{h}{2}(1 - \cos(\dfrac{2\pi v}{L_{bump}}t)), & 0 \le t \le 2\,\text{s}, \\ \displaystyle\sum_{n=N_{f_0}}^{N_f} s_n \sin(n\omega_0 t + \varphi_n), & t > 2\,\text{s}, \end{cases} \tag{75}$$

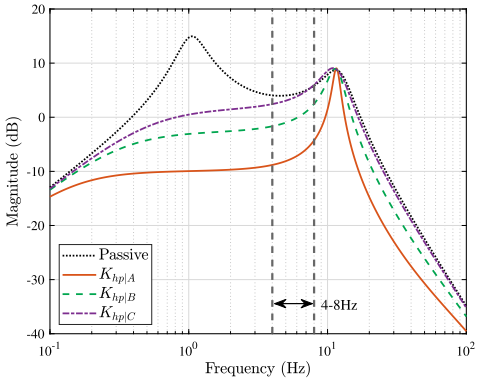

(a) Frequency responses of $\ddot{z}_c$

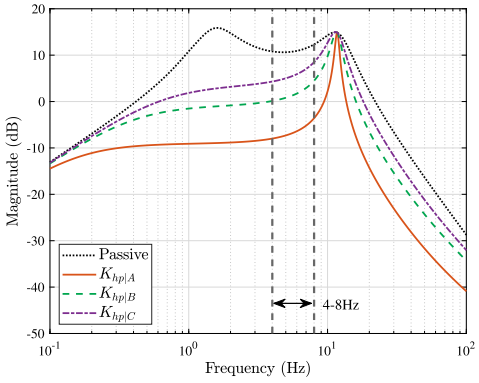

(b) Frequency responses of $\ddot{\theta}$

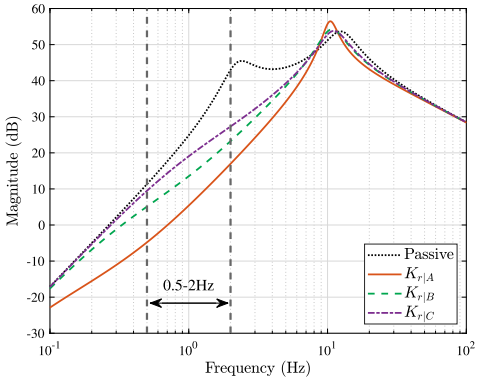

(c) Frequency responses of $\ddot{\phi}$

FIGURE 4. Frequency responses of heave acceleration $\ddot{z}_c$, pitch acceleration $\ddot{\theta}$, and roll acceleration $\ddot{\phi}$ for the selected optimal control gain matrices $\{K_{hp|A}, K_{r|A}\}$, $\{K_{hp|B}, K_{r|B}\}$ and $\{K_{hp|C}, K_{r|C}\}$.

$$\dot{z}_{r1}(t) = \begin{cases} \dfrac{h\nu\pi}{L_{bump}} \sin(\dfrac{2\pi\nu}{L_{bump}}t)), & 0 \le t \le 2\,\text{s}, \\ \displaystyle\sum_{n=N_{f_0}}^{N_f} s_n n\omega_0 \cos(n\omega_0 t + \varphi_n), & t > 2\,\text{s}, \end{cases} \tag{76}$$

where $h = 0.1$m is the height of the bump, $L_{bump} = 3.3$m is the length of the bump, and $\nu = 10$m/s is the vehicle's forward velocity. In the random vibration signal generated by PSD, $N_{f_0} = 5$ and $N_f = 80$ are the factors for limiting the frequency range, $\omega_0 := \frac{2\pi}{L_{psd}}\nu$ with the length of the road segment $L_{psd} = 100$ is the fundamental temporal frequency, and φ_n is the phase randomly chosen in the interval $[0, 2\pi]$. The amplitude of the excitation harmonic is defined as $s_n := \sqrt{2\Omega_h S_g(n\Omega_h)}$, where $\Omega_h := 2\pi/L_{psd}$ and the spectra $S_g(\Omega)$ corresponding to the geometrical profile of the road are approximated as follows: For a spatial frequency Ω,

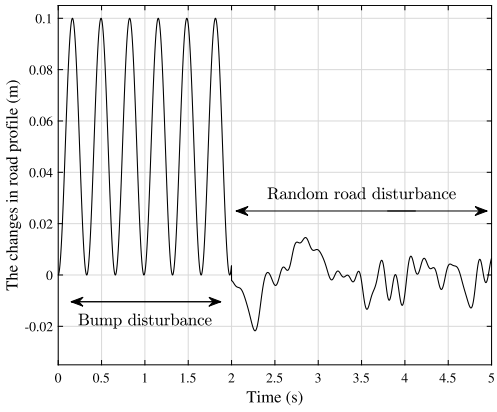

(a) Road displacement profile of z_{r1}

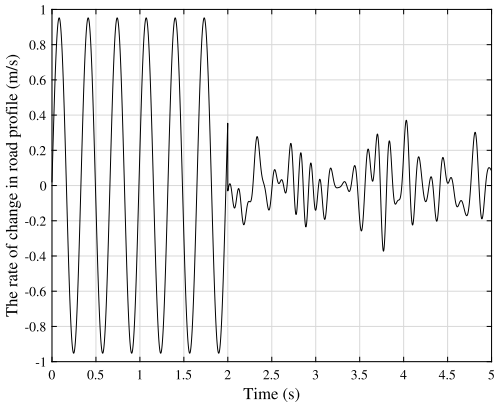

(b) Rate of change $\dot{z}_{r1}$ of z_{r1}

FIGURE 5. Time histories of the road profile and its rate of change for the front-right wheel.

$$S_g(\Omega) = \begin{cases} G_0 \left(\dfrac{\Omega}{\Omega_0}\right)^{-\psi_1}, & \text{if } \Omega \le \Omega_0, \\ G_0 \left(\dfrac{\Omega}{\Omega_0}\right)^{-\psi_2}, & \text{if } \Omega > \Omega_0, \end{cases} \tag{77}$$

where $\psi_1 = 2$, $\psi_2 = 1.5$, $\Omega_0 = 1/2\pi$, and $G_0 = 256 \times 10^{-6}\,\text{m}^3$ is the road roughness selected from ISO 8608 to be a bad quality of road roughness. Figure 5 shows the time histories of z_{r1} and $\dot{z}_{r1}$ generated by (75) and (76), respectively. The above road profile was applied to the front-right, front-left, rear-right, and rear-left wheels in turn, i.e., the front-left wheel was disturbed 0.1 s after the front-right wheel was affected by the road and the two rear wheels were disturbed $(l_f + l_r)/\nu$ s after the front wheels were affected by the road. Furthermore, the random road was constructed using the PSD signal within the 0.5–8-Hz frequency band to evaluate the performance of the controlled active suspension system.

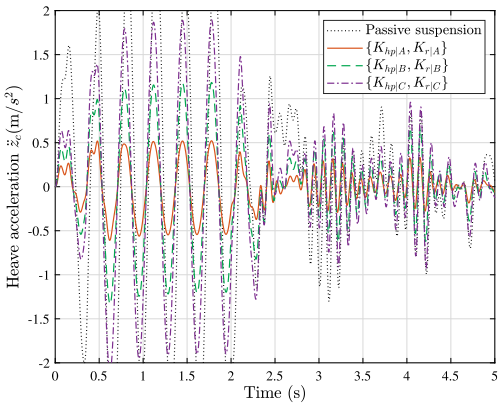

(a) Heave acceleration $\ddot{z}_c$

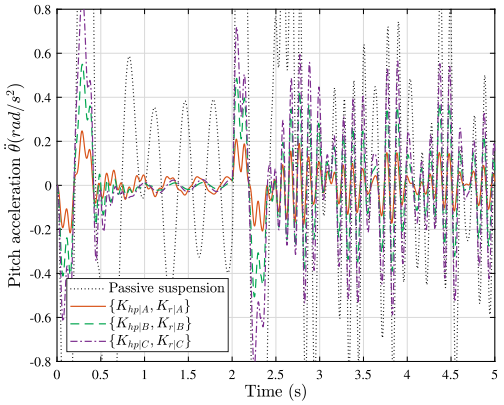

(b) Pitch acceleration $\ddot{\theta}$

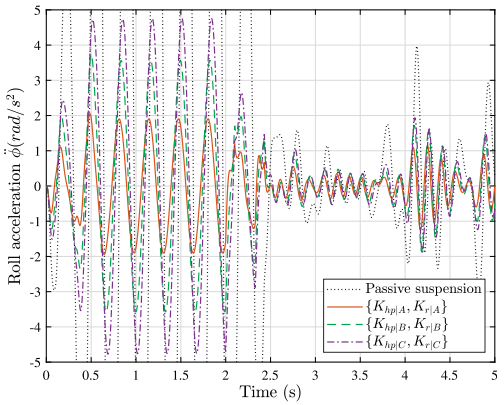

(c) Roll acceleration $\ddot{\phi}$

FIGURE 6. Time-domain responses of the sprung mass under bump and random road disturbances.

The time-domain responses of heave, pitch, and roll motions subject to the bump and random road disturbances shown in Figure 5 are plotted in Figure 6. Obviously, the active suspension system with the controller set $\{K_{hp|A}, K_{r|A}\}$ achieves better performance in heave, pitch, and roll directions compared with those using other sets of control gain matrices $\{K_{hp|B}, K_{r|B}\}$ and $\{K_{hp|C}, K_{r|C}\}$. Further, Figure 7 shows the time histories of the normalized suspension deflections ($z_{sd,hpf}/2z_{sd,max} \in \mathbf{z}_{2,hp}$, $z_{sd,hpr}/2z_{sd,max} \in \mathbf{z}_{2,hp}$, $z_{sd,rf}/2z_{sd,max} \in \mathbf{z}_{2,r}$, $z_{sd,rr}/2z_{sd,max} \in \mathbf{z}_{2,r}$) of the controlled active suspension system, where all of them are smaller than 1, indicating that the constraint conditions (16) are satisfied. As expected, the performance in terms of the suspension deflection corresponding to $\{K_{hp|A}, K_{r|A}\}$ is not superior to that of others using $\{K_{hp|B}, K_{r|B}\}$ and $\{K_{hp|C}, K_{r|C}\}$ because Case A yields a larger GH_2-norm value than Cases B and C do, as verified from Figure 3. Similarly, Figure 8 demonstrates that the control gain matrices $\{K_{hp|A}, K_{r|A}\}$ yield worse performance with respect to the normalized dynamic tire loads ($k_{tf}z_{td,hpf}/F_f \in \mathbf{z}_{2,hp}$ and $k_{tr}z_{td,hpr}/F_r \in \mathbf{z}_{2,hp}$) than $\{K_{hp|B}, K_{r|B}\}$ and $\{K_{hp|C}, K_{r|C}\}$. All control gain matrices guarantee the constraints (17)-(18) as shown in Figure 8. Finally, Figure 9 illustrates the time histories of four actuating forces (u_1, u_2, u_3, and u_4) required for controlling the full-vehicle active suspension system that works under bump and random road disturbances. The magnitudes of all actuator forces do not exceed their maximum of 6000N, which demonstrates that the constraint (21) related to the limitation of actuator force is guaranteed.

Finally, to demonstrate the superiority of the presented controller synthesis scheme, the conventional SOF controller design methods proposed by Du and Zhang [23] and Han and Zhao [24] are introduced. These conventional studies considered the entire-frequency H_∞/GH_2 controller design technique [23] and H_2/GH_2 controller design technique with a polytopic model [24]. Notably, their techniques for developing SOF controllers for vehicle-ride comfort enhancement were mainly based on a *single*-objective optimization problem aiming to minimize H_∞ or H_2 norms, i.e., their methods require a GH_2 norm that must be set in advance to some value by designers. Therefore, after fixing the GH_2 norm to 8 for the heave–pitch motion controller and 80 for the roll motion controller, the conventional controller design methods [23], [24] were applied, which yielded the following sets of control gain matrices:

$$\begin{cases} K_{hp,[23]} = \begin{bmatrix} -298.84 & -118.30 & -220.28 & -265.96 \\ 297.99 & -150.80 & 461.81 & -177.27 \end{bmatrix} \times 10^3, \\ K_{r,[23]} = \begin{bmatrix} -251.02 & -116.74 & -101.690 \\ -73.75 & -102.44 & -25.79 \end{bmatrix} \times 10^3, \end{cases} \tag{78}$$

$$\begin{cases} K_{hp,[24]} = \begin{bmatrix} -307.38 & -214.30 & -244.98 & -363.42 \\ 255.15 & -138.24 & 374.21 & -295.58 \end{bmatrix} \times 10^3, \\ K_{r,[24]} = \begin{bmatrix} -227.62 & -179.81 & -168.20 \\ -186.30 & -249.52 & -177.36 \end{bmatrix} \times 10^3. \end{cases} \tag{79}$$

For a fair comparison, the following control gain matrix pair yielding GH_2 norms approximately equal to 8 for heave–pitch motion and 80 for roll motion was selected from

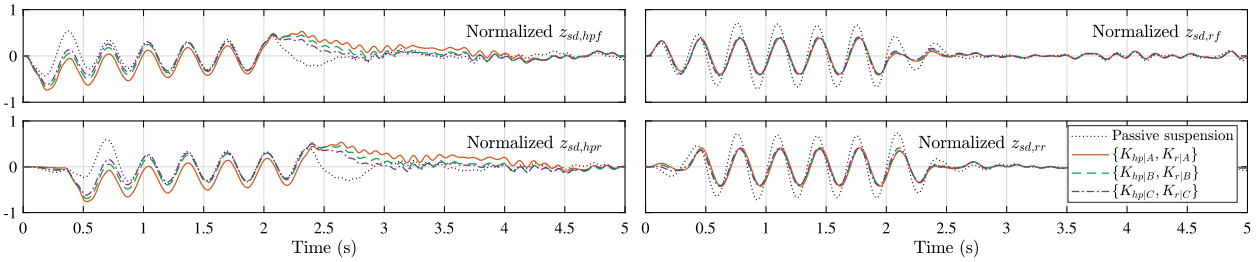

FIGURE 7. Time histories of normalized suspension deflections of a full-vehicle nominal model under bump and random road disturbances: (Top-left) $z_{sd,hpf}/2z_{sd,max}$, (Bottom-left) $z_{sd,hpr}/2z_{sd,max}$, (Top-right) $z_{sd,rf}/2z_{sd,max}$, (Bottom-right) $z_{sd,rr}/2z_{sd,max}$.

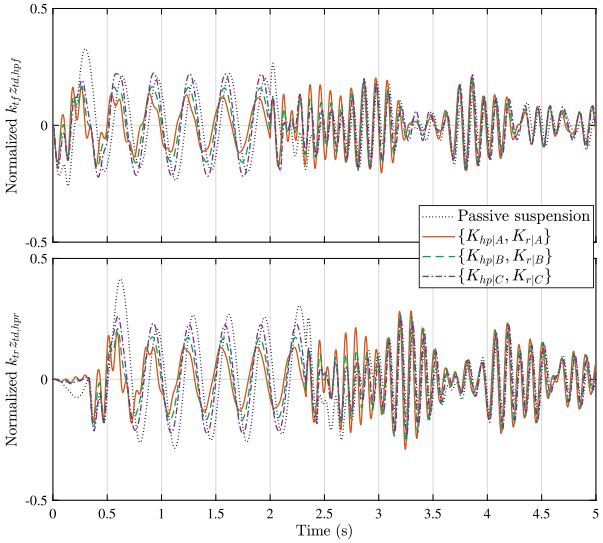

FIGURE 8. Time histories of normalized dynamic tire loads of a full-vehicle nominal model under bump and random road disturbances: (Top) $k_{tf}z_{td,hpf}/F_f$, (Bottom) $k_{tr}z_{td,hpr}/F_r$.

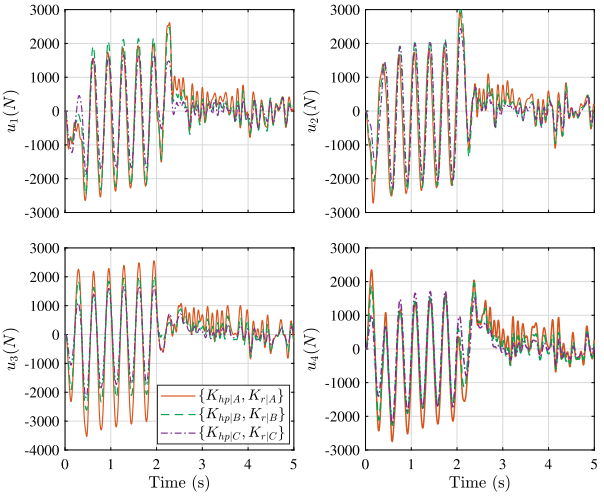

FIGURE 9. Time histories of four actuating forces of a full-vehicle nominal model under bump and random road disturbances.

TABLE 4. RMS values of pitch acceleration $\ddot{\theta}$ and roll acceleration $\ddot{\phi}$ weighted by ISO 2631 [19].

Control method	Signal	
	RMS of $\ddot{\theta}$	RMS of $\ddot{\phi}$
Passive suspension	0.4181	5.0472
Du and Zhang [23]	0.1142	2.4485
Han and Zhao [24]	0.1261	1.3276
This study	0.0773	0.7823

the Pareto-optimal set shown in Figure 3:

$$\begin{cases} K_{hp} = \begin{bmatrix} -355.37 & -77.86 & -384.02 & -65.49 \\ 244.13 & -383.37 & 160.82 & -451.60 \end{bmatrix} \times 10^3, \\ K_r = \begin{bmatrix} -40.75 & 37.53 & -26.49 \\ 70.28 & -9.41 & 3.33 \end{bmatrix} \times 10^3. \end{cases} \tag{80}$$

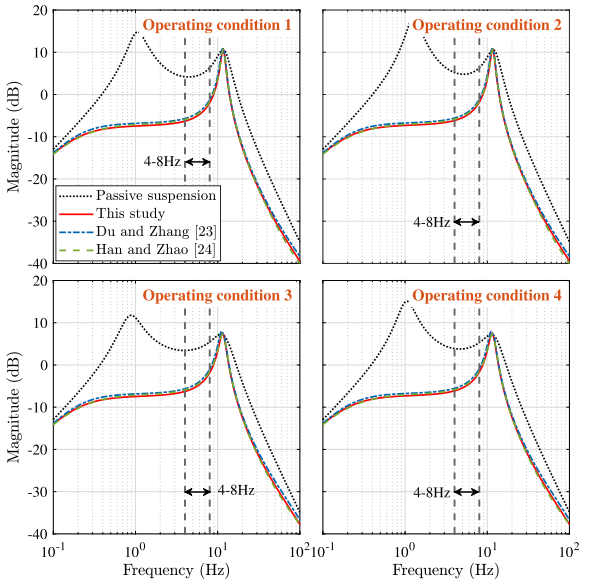

FIGURE 10. Frequency responses of heave acceleration $\ddot{z}_c$ under four operating conditions.

The following simulation results were performed for the full-vehicle active suspension system with the perturbed

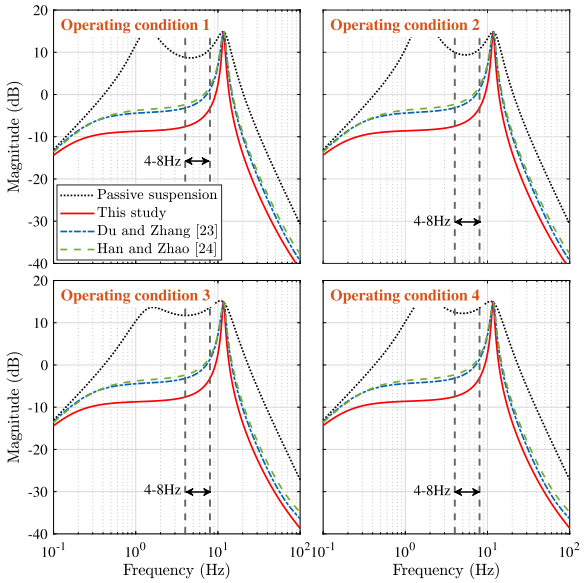

FIGURE 11. Frequency responses of pitch acceleration $\ddot{\theta}$ under four operating conditions.

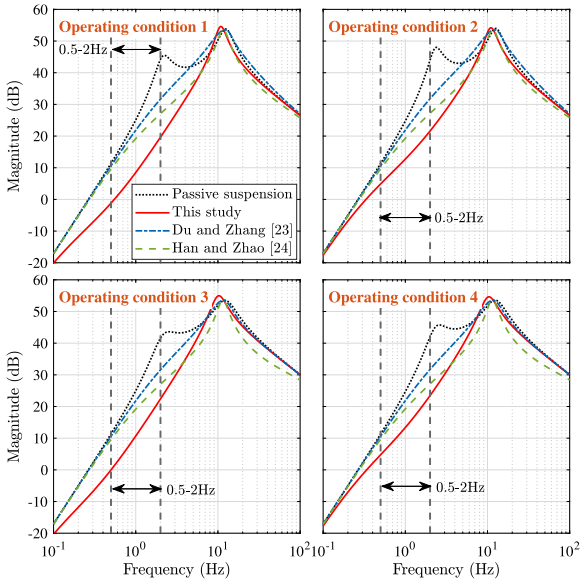

FIGURE 12. Frequency responses of roll acceleration $\ddot{\phi}$ under four operating conditions.

parameter values of $\{m_s, k_f, k_r, c_f, c_s\}$ given in Table 3 to validate the robustness against model parameter uncertainties. For active suspension systems, which were set according to different parameter values of operating conditions 1–4 from Table 3 and controlled by SOF controllers with different gain matrices in (78)-(80), the obtained closed-loop frequency response curves of heave, pitch, and roll accelerations are presented in Figures 10-12. Figure 10 indicates that all SOF controller gain matrix sets $\{K_{hp,[23]}, K_{r,[23]}\}$, $\{K_{hp,[24]}, K_{r,[24]}\}$, and $\{K_{hp}, K_r\}$ exhibit similar performances over the entire frequency band in terms of the frequency responses of heave acceleration $\ddot{z}_c$. By contrast, the frequency responses of pitch

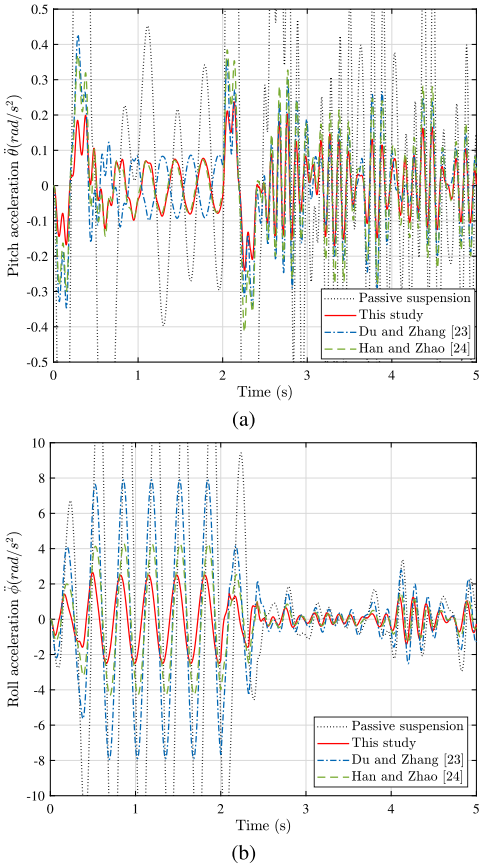

FIGURE 13. Time histories of (a) pitch acceleration $\ddot{\theta}$ and (b) roll acceleration $\ddot{\phi}$ of a full-vehicle active suspension system with perturbed parameters of operating condition 1.

and roll accelerations shown in Figures 11-12 clearly demonstrate that our control gain matrix pair $\{K_{hp}, K_r\}$ outperforms the other two sets of gain matrices $\{K_{hp,[23]}, K_{r,[23]}\}$ and $\{K_{hp,[24]}, K_{r,[24]}\}$, particularly in the frequency ranges of 4–8 Hz for pitch motion and 0.5–2 Hz for roll motion. To reconfirm the superiority of our controllers with $\{K_{hp}, K_r\}$ from the viewpoint of vehicle-ride quality in the time domain, the full-vehicle active suspension system was assumed to experience the successive excitation of bump and random road profiles illustrated in Figure 5. The simulation results are plotted in Figure 13 and show that the controllers with $\{K_{hp}, K_r\}$ achieve better performances in both pitch- and roll-directional motions compared with the others using $\{K_{hp,[23]}, K_{r,[23]}\}$ and $\{K_{hp,[24]}, K_{r,[24]}\}$. Meanwhile, vehicle-ride comfort can be well quantified by the RMS values of the accelerations weighted according to ISO 2631 [19]. The RMS value of an n-dimensional weighted acceleration vector $\mathcal{X}$ is calculated by $\mathcal{X}_{RMS} = \sqrt{\frac{1}{n}\sum_{j=1}^{n}\mathcal{X}_j^2}$. The RMS values of the weighted pitch acceleration $\ddot{\theta}$ and roll acceleration $\ddot{\phi}$ for different control methods are given in Table 4, where our controllers with $\{K_{hp}, K_r\}$ yield better performances in both pitch and roll motions compared with those developed using conventional methods [23], [24]. Because the com-

pared control gain matrix pairs $\{K_{hp}, K_r\}$ $\{K_{hp,[23]}, K_{r,[23]}\}$ and $\{K_{hp,[24]}, K_{r,[24]}\}$ yield approximately equal GH_2 norms, their time histories of suspension deflections, dynamic tire loads, and actuating forces are almost identical. The above examinations clearly verify that the full-vehicle active suspension system controlled by the proposed finite-frequency SOF H_∞/GH_2 control scheme achieves better performance on heave, pitch, and roll motions even if vehicle parameter uncertainties exist. Thus, the superiority of the proposed finite-frequency SOF H_∞/GH_2 control synthesis using the multi-objective metaheuristic optimizer is verified.

VI. CONCLUSION

In this paper, a multi-objective H_∞/GH_2 SOF controller is proposed for a 7-DOF full-vehicle active suspension system. To design a controlled system that performs satisfactorily under a wide range of road irregularities, the GKYP lemma is adopted such that the targeted disturbance attenuation for H_∞ performance-related ride comfort in specific frequency bands—4–8Hz for vertical motion and 0.5–2Hz for transversal motion— is realized. Moreover, practical constraints such as the suspension deflection limitation, road-holding ability, and actuator saturation required for manipulating the active suspension are handled by the GH_2 performance measure. Because of the difficulties in resolving such a multi-objective SOF control problem subject to nonconvex BMIs, the multi-objective quantum-behaved PSO algorithm is developed to efficiently explore the relevant trade-offs among the considered multiple performance objectives and eventually provide the desired Pareto-optimal control set. The designed H_∞/GH_2 SOF controllers are validated through numerical simulations on both bump and random road disturbances. The results demonstrate that the optimized H_∞/GH_2 SOF controller with the limited-frequency characteristic realizes better overall active suspension performances compared with conventional SOF controllers. The extension of this multi-objective H_∞/GH_2 SOF control scheme for robustness against actuator faults will be investigated in a future study.

APPENDIX A
STATE-SPACE REPRESENTATION OF THE HEAVE–PITCH MOTION

The state-space representation of heave/pitch motion is derived here. From (6)-(9), the accelerations of the sprung mass for the state variables of heave/pitch motion are represented as follows:

$$\ddot{z}_{s,hpf} = \ddot{z}_{s1} + \ddot{z}_{s2} \approx 2\ddot{z}_c - 2l_f\ddot{\theta}, \tag{81}$$
$$\ddot{z}_{s,hpr} = \ddot{z}_{s3} + \ddot{z}_{s4} \approx 2\ddot{z}_c + 2l_r\ddot{\theta}. \tag{82}$$

Then, substituting the dynamic equations (1)-(2) into the above equations, the accelerations $\ddot{z}_{s,hpf}$ and $\ddot{z}_{s,hpr}$ can be rewritten as follows:

$$\ddot{z}_{s,hpf} = \frac{2}{m_s}(f_1 + f_2 + f_3 + f_4) - \frac{2l_f}{I_y}\{-l_f(f_1 + f_2) + l_r(f_3 + f_4)\}, \tag{83}$$

$$\ddot{z}_{s,hpr} = \frac{2}{m_s}(f_1 + f_2 + f_3 + f_4) + \frac{2l_r}{I_y}\{-l_f(f_1 + f_2) + l_r(f_3 + f_4)\}. \tag{84}$$

Defining $a_1 := \frac{1}{m_s} + \frac{l_f^2}{I_y}$, $a_2 := \frac{1}{m_s} - \frac{l_f l_r}{I_y}$, and $a_3 := \frac{1}{m_s} + \frac{l_r^2}{I_y}$, (83) and (84) become

$$\ddot{z}_{s,hpf} = 2a_1(f_1 + f_2) + 2a_2(f_3 + f_4), \tag{85}$$
$$\ddot{z}_{s,hpr} = 2a_2(f_1 + f_2) + 2a_3(f_3 + f_4). \tag{86}$$

Let the ℓ-th entry of a vector $\mathcal{X}$ be denoted by $\mathcal{X}[\ell]$. From (4), $\dot{\boldsymbol{x}}_{hp}[1]$ and $\dot{\boldsymbol{x}}_{hp}[2]$ can be derived as follows:

$$\begin{aligned}\dot{\boldsymbol{x}}_{hp}[1] &= \ddot{z}_{s,hpf} \\ &= 2a_1(-c_f\dot{z}_{s,hpf} - k_f z_{sd,hpf} + c_f\dot{z}_{u,hpf} + u_{hpf}) \\ &\quad + 2a_2(-c_r\dot{z}_{s,hpr} - k_r z_{sd,hpr} + c_r\dot{z}_{u,hpr} + u_{hpr}),\end{aligned} \tag{87}$$

$$\begin{aligned}\dot{\boldsymbol{x}}_{hp}[2] &= \ddot{z}_{s,hpr} \\ &= 2a_2(-c_f\dot{z}_{s,hpf} - k_f z_{sd,hpf} + c_f\dot{z}_{u,hpf} + u_{hpf}) \\ &\quad + 2a_3(-c_r\dot{z}_{s,hpr} - k_r z_{sd,hpr} + c_r\dot{z}_{u,hpr} + u_{hpr}).\end{aligned} \tag{88}$$

Moreover, the velocity of suspension deflection related to heave/pitch motion is simply represented by the heave/pitch state variables as follows:

$$\dot{\boldsymbol{x}}_{hp}[3] = \dot{z}_{sd,hpf} = \dot{z}_{s,hpf} - \dot{z}_{u,hpf}, \tag{89}$$
$$\dot{\boldsymbol{x}}_{hp}[4] = \dot{z}_{sd,hpr} = \dot{z}_{s,hpr} - \dot{z}_{u,hpr}. \tag{90}$$

The acceleration of the unsprung mass for heave/pitch motion can be obtained using the aforementioned definition as follows:

$$\ddot{z}_{u,hpf} = \ddot{z}_{u1} + \ddot{z}_{u2}, \tag{91}$$
$$\ddot{z}_{u,hpr} = \ddot{z}_{u3} + \ddot{z}_{u4}. \tag{92}$$

From (12)-(15), $\ddot{z}_{u,hpf}$ and $\ddot{z}_{u,hpr}$ can be replaced with the following equations:

$$\begin{aligned}\ddot{z}_{u,hpf} &= \frac{1}{m_1}(-f_1 - k_{t1}z_{td,1} - \frac{M_{abf}}{l_w}) \\ &\quad + \frac{1}{m_2}(-f_2 - k_{t2}z_{td,2} + \frac{M_{abf}}{l_w}) \\ &= \frac{1}{m_f}(-f_1 - f_2 - k_{tf}z_{td,hpf}),\end{aligned} \tag{93}$$

$$\begin{aligned}\ddot{z}_{u,hpr} &= \frac{1}{m_3}(-f_3 - k_{t3}z_{td,3} - \frac{M_{abr}}{l_w}) \\ &\quad + \frac{1}{m_4}(-f_4 - k_{t4}z_{td,4} + \frac{M_{abr}}{l_w}) \\ &= \frac{1}{m_r}(-f_3 - f_4 - k_{tr}z_{td,hpr}).\end{aligned} \tag{94}$$

By substituting (4) into the above equations, the accelerations of the unsprung mass comprising state variables for heave/pitch motion can be derived as follows:

$$\dot{\boldsymbol{x}}_{hp}[5] = \ddot{z}_{u,hpf}$$

$$= \frac{1}{m_f}(c_f\dot{z}_{s,hpf} + k_f z_{sd,hpf} - c_f\dot{z}_{u,hpf} - k_{tf}z_{td,hpf} - u_{hpf}), \quad (95)$$

$$\dot{\boldsymbol{x}}_{hp}[6] = \ddot{z}_{u,hpr} = \frac{1}{m_r}(c_r\dot{z}_{s,hpr} + k_r z_{sd,hpr} - c_r\dot{z}_{u,hpr} - k_{tr}z_{td,hpr} - u_{hpr}). \quad (96)$$

The velocity of tire deflection in the heave/pitch motion is simply obtained as follows:

$$\dot{\boldsymbol{x}}_{hp}[7] = \dot{z}_{td,hpf} = \dot{z}_{u,hpf} - \dot{z}_{r,hpf}, \quad (97)$$

$$\dot{\boldsymbol{x}}_{hp}[8] = \dot{z}_{td,hpr} = \dot{z}_{u,hpr} - \dot{z}_{r,hpr}. \quad (98)$$

APPENDIX B
PERFORMANCE OUTPUT EQUATIONS FOR HEAVE–PITCH MOTION

The variables of the performance output vector related to heave–pitch motion are derived here. The heave–pitch acceleration $\boldsymbol{z}_{1,hp}$ is developed from (1) and (2) as follows:

$$\boldsymbol{z}_{1,hp}[1] = q_1\ddot{z}_c = \frac{q_1}{m_s}(f_1 + f_2 + f_3 + f_4), \quad (99)$$

$$\boldsymbol{z}_{1,hp}[2] = q_2\ddot{\theta} = \frac{q_2}{I_y}\{-l_f(f_1 + f_2) + l_r(f_3 + f_4)\}. \quad (100)$$

Then, the above equations can be rewritten using (4) as

$$\boldsymbol{z}_{1,hp}[1] = \frac{q_1}{m_s}(-c_f\dot{z}_{s,hpf} - c_r\dot{z}_{s,hpr} - k_f z_{sd,hpf} - k_r z_{sd,hpr} + c_f\dot{z}_{u,hpf} + c_r\dot{z}_{u,hpr} + u_{hpf} + u_{hpr}), \quad (101)$$

$$\boldsymbol{z}_{1,hp}[2] = \frac{q_2}{I_y}\{-l_f(-c_f\dot{z}_{s,hpf} - k_f z_{sd,hpf} + c_f\dot{z}_{u,hpf} + u_{hpf}) + l_r(-c_r\dot{z}_{s,hpr} - k_r z_{sd,hpr} + c_r\dot{z}_{u,hpr} + u_{hpr})\}. \quad (102)$$

Further, the performance output variables for handling constraints, $\boldsymbol{z}_{2,hp}$, can be derived from the constraints (16), (17), (18), and (21) as follows:

$$-2z_{sd,\max} \le z_{sd1}(t) + z_{sd2}(t) \le 2z_{sd,\max}, \quad (103)$$

$$-2z_{sd,\max} \le z_{sd3}(t) + z_{sd4}(t) \le 2z_{sd,\max}, \quad (104)$$

$$k_{tf}z_{td,hpf}(t) \le F_f, \quad (105)$$

$$k_{tr}z_{td,hpr}(t) \le F_r, \quad (106)$$

$$-2u_{\max} \le u_1(t) + u_2(t) \le 2u_{\max}, \quad (107)$$

$$-2u_{\max} \le u_3(t) + u_4(t) \le 2u_{\max}. \quad (108)$$

Then, $\boldsymbol{z}_{2,hp}$ is represented by normalization as

$$\boldsymbol{z}_{2,hp} = \left[[\boldsymbol{z}_{2,hp}]_{11}\ [\boldsymbol{z}_{2,hp}]_{12}\ [\boldsymbol{z}_{2,hp}]_{13}\right]^T,$$
$$[\boldsymbol{z}_{2,hp}]_{11} = \left[\frac{z_{sd,hpf}}{2z_{sd,\max}}\ \frac{z_{sd,hpr}}{2z_{sd,\max}}\right],$$
$$[\boldsymbol{z}_{2,hp}]_{12} = \left[\frac{k_{tf}z_{td,hpf}}{F_f}\ \frac{k_{tr}z_{td,hpr}}{F_r}\right],$$
$$[\boldsymbol{z}_{2,hp}]_{13} = \left[\frac{u_{hpf}}{2u_{\max}}\ \frac{u_{hpr}}{2u_{\max}}\right]. \quad (109)$$

APPENDIX C
STATE-SPACE REPRESENTATION FOR ROLL MOTION

The state-space representation related to roll motion is derived here. The velocities of the variables such as $\dot{z}_{u,rf}$, $\dot{z}_{u,rr}$, and $\dot{\phi}$ can be represented by the state variables for roll motion as follows:

$$\dot{\boldsymbol{x}}_r[1] = \dot{z}_{u,rf} = \boldsymbol{x}_r[4], \quad (110)$$

$$\dot{\boldsymbol{x}}_r[2] = \dot{z}_{u,rr} = \boldsymbol{x}_r[5], \quad (111)$$

$$\dot{\boldsymbol{x}}_r[3] = \dot{\phi} = \boldsymbol{x}_r[6]. \quad (112)$$

Furthermore, $\ddot{z}_{u,rf}$ and $\ddot{z}_{u,rr}$—the accelerations of the unsprung mass for roll motion—can be derived from (12) and (15) as

$$\ddot{z}_{u,rf} = -\ddot{z}_{u1} + \ddot{z}_{u2} = \frac{1}{m_1}\left\{f_1 + k_{t1}(z_{u1} - z_{r1}) + \frac{M_{abf}}{l_w}\right\} + \frac{1}{m_2}\left\{-f_2 - k_{t2}(z_{u2} - z_{r2}) + \frac{M_{abf}}{l_w}\right\}, \quad (113)$$

$$\ddot{z}_{u,rr} = -\ddot{z}_{u3} + \ddot{z}_{u4} = \frac{1}{m_3}\left\{f_3 + k_{t3}(z_{u3} - z_{r3}) + \frac{M_{abr}}{l_w}\right\} + \frac{1}{m_4}\left\{-f_4 - k_{t4}(z_{u4} - z_{r4}) + \frac{M_{abr}}{l_w}\right\}. \quad (114)$$

These equations can be rewritten using (4), (10), and (11) as follows:

$$\ddot{z}_{u,rf} = \frac{1}{m_f}\left\{k_f z_{s,rf} - k_f z_{u,rf} + c_f\dot{z}_{s,rf} - c_f\dot{z}_{u,rf} - u_{rf} - k_{tf}z_{u,rf} + k_{tf}z_{r,rf} + \frac{2k_{abf}}{l_w^2}(z_{s,rf} - z_{u,rf})\right\}, \quad (115)$$

$$\ddot{z}_{u,rr} = \frac{1}{m_r}\left\{k_r z_{s,rr} - k_r z_{u,rr} + c_r\dot{z}_{s,rr} - c_r\dot{z}_{u,rr} - u_{rr} - k_{tr}z_{u,rr} + k_{tr}z_{r,rr} + \frac{2k_{abr}}{l_w^2}(z_{s,rr} - z_{u,rr})\right\}. \quad (116)$$

The acceleration of the unsprung mass can be represented by the state variables for roll motion by the approximated equation $z_{s,rf} = z_{s,rr} \approx l_w\phi$ as follows:

$$\dot{\boldsymbol{x}}_r[4] = \ddot{z}_{u,rf} = \frac{1}{m_f}\left\{(-k_f - k_{tf} - \frac{2k_{abf}}{l_w^2})z_{u,rf} + (k_f l_w + \frac{2k_{abf}}{l_w})\phi - c_f\dot{z}_{u,rf} + c_f l_w\dot{\phi} + k_{tf}z_{r,rf} - u_{rf}\right\}, \quad (117)$$

$$\dot{\boldsymbol{x}}_r[5] = \ddot{z}_{u,rr} = \frac{1}{m_r}\left\{(-k_r - k_{tr} - \frac{2k_{abr}}{l_w^2})z_{u,rr} + (k_r l_w + \frac{2k_{abr}}{l_w})\phi - c_r\dot{z}_{u,rr} + c_r l_w\dot{\phi} + k_{tr}z_{r,rr} - u_{rr}\right\}. \quad (118)$$

From (3), the acceleration of roll motion is given as

$$\ddot{\phi} = \frac{1}{I_x}\left\{\frac{l_w}{2}(-f_1+f_2)+\frac{l_w}{2}(-f_3+f_4)-M_{abf}-M_{abr}\right\}. \tag{119}$$

Then, this equation can be rewritten using (4), (10) and (11) as

$$\begin{aligned}\ddot{\phi} = \frac{1}{I_x}\Bigg\{&\frac{l_w}{2}(-k_f z_{s,rf}+k_f z_{u,rf}-c_f\dot{z}_{s,rf}+c_f\dot{z}_{u,rf}+u_{rf})\\ &+\frac{l_w}{2}(-k_r z_{s,rr}+k_r z_{u,rr}-c_r\dot{z}_{s,rr}+c_r\dot{z}_{u,rr}+u_{rr})\\ &-\frac{k_{abf}}{l_w}(z_{s,rf}-z_{u,rf})-\frac{k_{abr}}{l_w}(z_{s,rr}-z_{u,rr})\Bigg\}.\end{aligned} \tag{120}$$

From the approximated equation $z_{s,rf} = z_{s,rr} \approx l_w\phi$, the acceleration of roll motion represented by the state variables can be expressed as

$$\begin{aligned}\dot{x}_r[6] = \ddot{\phi}&\\ = \frac{1}{I_x}\Bigg\{&(\frac{l_w k_f}{2}+\frac{k_{abf}}{l_w})z_{u,rf}+(\frac{l_w k_r}{2}+\frac{k_{abr}}{l_w})z_{u,rr}\\ &+(-\frac{l_w^2 k_f}{2}-\frac{l_w^2 k_r}{2}-k_{abf}-k_{abr})\phi+\frac{l_w c_f}{2}\dot{z}_{u,rf}\\ &+\frac{l_w c_r}{2}\dot{z}_{u,rr}+(-\frac{l_w^2 c_f}{2}-\frac{l_w^2 c_r}{2})\dot{\phi}+\frac{l_w}{2}u_{rf}\\ &+\frac{l_w}{2}u_{rr}\Bigg\}.\end{aligned} \tag{121}$$

APPENDIX D
PERFORMANCE OUTPUT EQUATIONS FOR ROLL MOTION

The performance output variables for roll motion are derived here. The acceleration of roll motion was selected as the variable of performance output vector as $z_{1,r} = [\ddot{\phi}]$; therefore, $z_{1,r}$ can be found from (119)–(121). Further, $z_{2,r}$, the controlled output vector related to the constraints for the roll system, can be derived from the constraints (16) and (21) as follows:

$$-2z_{sd,\max} \le -z_{sd1}(t)+z_{sd2}(t) \le 2z_{sd,\max}, \tag{122}$$
$$-2z_{sd,\max} \le -z_{sd3}(t)+z_{sd4}(t) \le 2z_{sd,\max}, \tag{123}$$
$$-2u_{\max} \le -u_1+u_2 \le 2u_{\max}, \tag{124}$$
$$-2u_{\max} \le -u_3+u_4 \le 2u_{\max}. \tag{125}$$

Then, the variables of the controlled output vector $z_{2,r}$ can be represented by normalized considerations as follows:

$$z_{2,r} = \left[\frac{z_{sd,rf}}{2z_{sd,\max}} \quad \frac{z_{sd,rr}}{2z_{sd,\max}} \quad \frac{u_{rf}}{2u_{max}} \quad \frac{u_{rr}}{2u_{max}}\right]^T. \tag{126}$$

REFERENCES

[1] Y. Huang, J. Na, X. Wu, X. Liu, and Y. Guo, "Adaptive control of nonlinear uncertain active suspension systems with prescribed performance," *ISA Trans.*, vol. 54, pp. 145–155, Jan. 2015.

[2] S. Chantranuwathana and H. Peng, "Adaptive robust control for active suspensions," in *Proc. Amer. Control Conf.*, vol. 3, Jun. 1999, pp. 1702–1706.

[3] T. Yoshimura, K. Nakaminami, M. Kurimoto, and J. Hino, "Active suspension of passenger cars using linear and fuzzy-logic controls," *Control Eng. Pract.*, vol. 7, no. 1, pp. 41–47, Jan. 1999.

[4] J. Cao, P. Li, and H. Liu, "An interval fuzzy controller for vehicle active suspension systems," *IEEE Trans. Intell. Transp. Syst.*, vol. 11, no. 4, pp. 885–895, Dec. 2010.

[5] K. Rajeswari and P. Lakshmi, "PSO optimized fuzzy logic controller for active suspension system," in *Proc. Int. Conf. Adv. Recent Technol. Commun. Comput.*, Oct. 2010, pp. 278–283.

[6] Y. M. Sam, M. R. H. A. Ghani, and N. Ahmad, "LQR controller for active car suspension," in *Proc. Intell. Syst. Technol. New Millennium*, vol. 1, Sep. 2000, pp. 441–444.

[7] H. D. Taghirad and E. Esmailzadeh, "Automobile passenger comfort assured through LQG/LQR active suspension," *J. Vib. Control*, vol. 4, no. 5, pp. 603–618, Sep. 1998.

[8] E. Alvarez-Sánchez, "A quarter-car suspension system: Car body mass estimator and sliding mode control," *Proc. Technol.*, vol. 7, pp. 208–214, Jan. 2013.

[9] C. Zhou, X. Liu, W. Chen, F. Xu, and B. Cao, "Optimal sliding mode control for an active suspension system based on a genetic algorithm," *Algorithms*, vol. 11, no. 12, p. 205, Dec. 2018.

[10] A. Orvnäs, S. Stichel, and R. Persson, "Active lateral secondary suspension with H_∞ control to improve ride comfort: Simulations on a full-scale model," *Vehicle Syst. Dyn.*, vol. 49, no. 9, pp. 1409–1422, 2011.

[11] T. P. J. van der Sande, B. L. J. Gysen, I. J. M. Besselink, J. J. H. Paulides, E. A. Lomonova, and H. Nijmeijer, "Robust control of an electromagnetic active suspension system: Simulations and measurements," *Mechatronics*, vol. 23, no. 2, pp. 204–212, Mar. 2013.

[12] H. Du, N. Zhang, and F. Naghdy, "Robust control of vehicle electrorheological suspension subject to measurement noises," *Vehicle Syst. Dyn.*, vol. 49, nos. 1–2, pp. 257–275, Feb. 2011.

[13] Y. Zhao, W. Sun, and H. Gao, "Robust control synthesis for seat suspension systems with actuator saturation and time-varying input delay," *J. Sound Vib.*, vol. 329, no. 21, pp. 4335–4353, Oct. 2010.

[14] C. Wei, Y. Cai, K. Zhang, Z. Wang, and W. Yu, "Novel optimal design approach for output-feedback H_∞ control of vehicle active seat-suspension system," *Asian J. Control*, vol. 22, no. 1, pp. 411–422, Jan. 2020.

[15] H. Chen, P.-Y. Sun, and K.-H. Guo, "Constrained H-infinity control of active suspensions: An LMI approach," in *Proc. Int. Conf. Control Automat., Final Program Book Abstr.*, Jun. 2002, p. 157.

[16] H. Chen, Z.-Y. Liu, and P.-Y. Sun, "Application of constrained H_∞ control to active suspension systems on half-car models," *J. Dyn. Syst., Meas., Control*, vol. 127, no. 3, pp. 345–354, Sep. 2005, doi: 10.1115/1.1985442.

[17] G. Wang, C. Chen, and S. Yu, "Optimization and static output-feedback control for half-car active suspensions with constrained information," *J. Sound Vib.*, vol. 378, pp. 1–13, Sep. 2016.

[18] H. Jing, R. Wang, C. Li, and J. Bao, "Robust finite-frequency H_∞ control of full-car active suspension," *J. Sound Vib.*, vol. 441, pp. 221–239, Feb. 2019.

[19] *Mechanical Vibration and Shock Evaluation of Human Exposure to Whole-Body Vibration Part 1: General Requirements*, ISO Standard 2631-1, 1997.

[20] W. Sun, J. Li, Y. Zhao, and H. Gao, "Vibration control for active seat suspension systems via dynamic output feedback with limited frequency characteristic," *Mechatronics*, vol. 21, no. 1, pp. 250–260, Feb. 2011.

[21] T. Iwasaki and S. Hara, "Generalized KYP Lemma: Unified frequency domain inequalities with design applications," *IEEE Trans. Autom. Control*, vol. 50, no. 1, pp. 41–59, Jan. 2005.

[22] H. Taghavifar and S. Rakheja, "Multi-objective optimal robust seat suspension control of off-road vehicles in the presence of disturbance and parametric uncertainty using metaheuristics," *IEEE Trans. Intell. Vehicles*, vol. 5, no. 3, pp. 372–384, Sep. 2020.

[23] H. Du and N. Zhang, "Designing H_∞/GH_2 static-output feedback controller for vehicle suspensions using linear matrix inequalities and genetic algorithms," *Vehicle Syst. Dyn.*, vol. 46, no. 5, pp. 385–412, May 2008.

[24] C. Han and D. Zhao, "Multi-objective static output feedback control for vehicle active suspension," in *Proc. IEEE Int. Conf. Mechatronics Autom.*, Aug. 2014, pp. 1526–1532.

[25] R. N. Jazar, *Vehicle Dynamics: Theory and Application*. New York, NY, USA: Springer 2008.

[26] R. Rajamani, *Vehicle Dynamics and Control*. New York, NY, USA: Springer 2006.

[27] D. Hrovat, "Survey of advanced suspension developments and related optimal control applications," *Automatica*, vol. 33, no. 10, pp. 1781–1817, 1997.

[28] U. Shaked, "An LPD approach to robust H_2 and H_∞ static output-feedback design," *IEEE Trans. Autom. Control.*, vol. 48, no. 5, pp. 866–872, May 2003.
[29] H. Du, K. Y. Sze, and J. Lam, "Semi-active H_∞ control of vehicle suspension with magneto-rheological dampers," *J. Sound Vib.*, vol. 283, nos. 3–5, pp. 981–996, 2005.
[30] A. Sadeghzadeh, "Fixed-order $\mathcal{H}_2$ controller design for state space polytopic systems," *Int. J. Control, Autom. Syst.*, vol. 12, no. 2, pp. 316–323, Apr. 2014, doi: 10.1007/s12555-013-0256-9.
[31] L. B. R. R. Romão, M. C. de Oliveira, P. L. D. Peres, and R. C. L. F. Oliveira, "State-feedback and filtering problems using the generalized KYP lemma," in *Proc. IEEE Conf. Comput. Aided Control Syst. Design (CACSD)*, Sep. 2016, pp. 1054–1059.
[32] M. A. Rotea, "The generalized H_2 control problem," *Automatica*, vol. 29, no. 2, pp. 373–385, Mar. 1993.
[33] A. Rodríguez-Molina, E. Mezura-Montes, M. G. Villarreal-Cervantes, and M. Aldape-Pérez, "Multi-objective meta-heuristic optimization in intelligent control: A survey on the controller tuning problem," *Appl. Soft Comput.*, vol. 93, Aug. 2020, Art. no. 106342.
[34] I. Maruta, T.-H. Kim, and T. Sugie, "Fixed-structure H_8 controller synthesis: A meta-heuristic approach using simple constrained particle swarm optimization," *Automatica*, vol. 45, no. 2, pp. 553–559, Feb. 2009.
[35] Y. Kong, D. Zhao, B. Yang, T. Shen, H. Li, and K. Han, "Static output feedback control for active suspension using PSO-DE/LMI approach," in *Proc. IEEE Int. Conf. Mechatronics Autom.*, Aug. 2012, pp. 366–370.
[36] C. A. C. Coello and M. S. Lechuga, "MOPSO: A proposal for multiple objective particle swarm optimization," in *Proc. Congr. Evol. Comput. (CEC)*, vol. 2, Jun. 2002, pp. 1051–1056.
[37] B. Luitel and G. K. Venayagamoorthy, "A PSO with quantum infusion algorithm for training simultaneous recurrent neural networks," in *Proc. Int. Joint Conf. Neural Netw.*, Jun. 2009, pp. 1923–1930, doi: 10.1109/IJCNN.2009.5179082.
[38] Y. Hwang, Y.-R. Ko, Y. Lee, and T.-H. Kim, "Frequency-domain tuning of robust fixed-structure controllers via quantum-behaved particle swarm optimizer with cyclic neighborhood topology," *Int. J. Control, Autom. Syst.*, vol. 16, no. 2, pp. 426–436, Apr. 2018, doi: 10.1007/s12555-016-0766-3.
[39] T.-H. Kim, I. Maruta, and T. Sugie, "A simple and efficient constrained particle swarm optimization and its application to engineering design problems," *Proc. Inst. Mech. Eng., C, J. Mech. Eng. Sci.*, vol. 224, no. 2, pp. 389–400, Feb. 2010, doi: 10.1243/09544062JMES1732.
[40] A. Agharkakli, G. Shafiei Sabet, and A. Barouz, "Simulation and analysis of passive and active suspension system using quarter car model for different road profile," *Int. J. Emerg. Trends Technol. Comput. Sci.*, vol. 3, no. 5, pp. 636–644, Jan. 2012.
[41] G. Verros, S. Natsiavas, and C. Papadimitriou, "Design optimization of quarter-car models with passive and semi-active suspensions under random road excitation," *J. Vib. Control*, vol. 11, no. 5, pp. 581–606, May 2005, doi: 10.1177/1077546305052315.

YEONGJAE KIM received the B.S. degree in mechanical engineering from Chung-Ang University, South Korea, in 2021, where he is currently pursuing the master's degree. His research interests include robust control, meta-heuristic optimization, multi-objective optimization, and controller design for active suspension systems.

TAEHEON KWAK received the B.S. degree in mechanical engineering from Chung-Ang University, South Korea, in 2021, where he is currently pursuing the master's degree. His research interests include dynamical multi-agent systems, optimization-based system identification, and control theoretic analysis.

MASAAKI KANNO received the bachelor's degree in mechanical engineering and the master's degree in information engineering from The University of Tokyo, in 1991 and 1993, respectively, the M.Phil. degree in control engineering from the University of Sussex, Brighton, U.K., in 2000, and the Ph.D. degree in control engineering from the University of Cambridge, Cambridge, U.K., in 2004. He joined Niigata University, in 2009. He is currently an Associate Professor. His research interests include the characterization of performance limitations in control, symbolic-numeric hybrid optimization for controller design, and guaranteed accuracy computation in control.

TAE-HYOUNG KIM (Member, IEEE) received the B.S. and M.S. degrees in mechanical engineering from Chung-Ang University, South Korea, in 1999 and 2001, respectively, and the Ph.D. degree in informatics from Kyoto University, Japan, in 2006. He is currently a Professor with the School of Mechanical Engineering, Chung-Ang University. His current research interests include robust control, multi-agent systems, meta-heuristic optimization, system identification, model predictive control, iterative learning control, and systems biology.